Geosci. Model Dev., 19, 2691–2716, 2026
https://doi.org/10.5194/gmd-19-2691-2026

Geoscientific Model Development
Open Access
EGU

Machine learning-driven characterization and prescription of aerosol optical properties for atmospheric models

Nilton Évora do Rosário[1], Karla M. Longo[2], Pedro H. Toso[1], Saulo R. Freitas[2], Marcia A. Yamasoe[3], Luiz Flávio Rodrigues[2], Otavio Medeiros[2], Haroldo Campos Velho[2], Isilda da Cunha Menezes[4], and Ana Isabel Miranda[4]

[1]Departamento de Ciências Ambientais, Universidade Federal de São Paulo, Diadema, SP, Brazil
[2]Instituto Nacional de Pesquisas Espaciais (INPE), São José dos Campos, SP, Brazil
[3]Departamento de Ciências Atmosféricas, Instituto de Astronomia, Geofísica e Ciências Atmosféricas, Universidade de São Paulo, Cidade Universitária, São Paulo, SP, Brazil
[4]Center for Environmental and Marine Studies (CESAM), Department of Environment and Planning, University of Aveiro, Campus Universitário de Santiago, 3810-193 Aveiro, Portugal

Correspondence: Nilton Évora do Rosário (nrosario@unifesp.br)

Received: 30 January 2025 – Discussion started: 16 April 2025
Revised: 5 March 2026 – Accepted: 17 March 2026 – Published: 10 April 2026

Abstract. Accurate modeling of aerosol optical properties is critical to simulate aerosol radiative effects. However, uncertainties regarding the simulation of aerosol-intensive optical properties are still significant. Therefore, the use of observations to constrain aerosol optical properties in models has been indicated as an option. Also, explicit computations of optical properties are still too costly for operational models, which makes observation-based prescriptions a convenient solution. We developed an observation-based prescription of aerosol optical properties driven by machine-learning techniques that can be applied in models. The Iberian Peninsula (IP) was taken as the reference domain, and the aerosol products from the AERONET sites across the IP were the main dataset. First, clustering was applied to define the typical aerosol optical regimes affecting the IP atmosphere. Five typical regimes were identified. Two of them were dominated by coarse mode, which was associated with Saharan dust. One was found to be close to pure dust, while the other indicated a mixed scenario of dust and pollution. Two of the non-dust regimes, strongly and moderately absorbing, were found to be associated with smoke. The remaining non-dust regime, with no clear association, occurs mostly in the eastern portion of the IP. Afterward, using aerosol-type columnar mass density from MERRA-2, a model was trained as a predictor of the optical regimes using the Random Forest method. The model was tested under distinct aerosol scenarios. Predictions' accuracy ranged from 60 % to 75 %, depending on the regime, while presenting an average accuracy of 70 %.

1 Introduction

The importance of aerosols in the Earth's climate system is undisputed. Aerosol particles participate directly in the planetary energy budgets via the scattering and absorption of terrestrial and solar radiation (Kim and Ramanathan, 2008; IPCC, 2021; Li et al., 2022). However, this participation is permeated by high complexity due to the variety of aerosol particles sizes and composition, which cause significant uncertainty (Spencer et al., 2019; IPCC, 2021; Li et al., 2022). The uncertainties and challenges in accurately representing aerosol particles' processes in climate, weather, and environmental models arise from various limitations. For instance, when it comes to aerosol direct interaction with radiation, the current global aerosol monitoring system does not provide a comprehensive spatial-temporal characterization of spectral complex refractive index and size distribution of the aerosol particles, critical information to characterize the particle absorption and scattering (Samset et al., 2018; Li et al., 2022). This lack of observational data contributes significantly to uncertainty in aerosol modeling and, therefore, to the uncertainty of the aerosol radiative forcing.

The difficulty of traditional libraries of aerosol optical and microphysical properties (Shettle and Fenn, 1979; Koepke et al., 1997; Hess et al., 1998) to describe geographical variation aerosol properties, for instance, soil dust mineralogy (Adebiyi et al., 2023), has been central in the aerosol optical properties uncertainty debate. Another critical aspect is the characterization of the state of the mixture of the aerosol particles in the model's aerosol modules (Samset et al., 2018; Sand et al., 2021). Given the complex dynamic of aerosol particle emission, transport, and removal in the atmosphere, numerical modelling of the state of the mixture and the resultant complex refractive index and size distribution is widely recognized as one of the most important sources of uncertainty in addressing aerosol particles' radiative forcing (Sand et al., 2021). According to Sand et al. (2021), aerosol absorption is poorly constrained, and the current climate models present a large range in the quantification of the main absorbing aerosol species – black carbon (BC), organic aerosols (OA), and mineral dust. Brown et al. (2021) findings indicate that biomass-burning aerosols in most climate models are too absorbing, mainly due to treatments of aerosol mixing state. They found the internal mixing assumptions used in climate models to overestimate Black Carbon (BC) absorption when compared to the observations. Saharan dust, a critical component of the global aerosol system, has been found to absorb less solar radiation than models estimate (Adebiyi et al., 2023), and the primary cause pointed out is the models' overestimation of the dust imaginary refractive index. Absorption is not the only issue facing aerosol particle representation in climate models; the relative contribution of fine and coarse mode particles is also a challenge. For instance, Adebiyi et al. (2023) also found models underestimating large dust particles when representing North African dust plumes.

Observation-constrained models have been recommended to mitigate models' current difficulty in fully simulating aerosol properties and processes accurately (Samset et al., 2018; Proske et al., 2024). In addition to the uncertainty aspects, explicit simulation of aerosol composition and microphysical properties, followed by explicit computation of intensive optical properties, is still too expensive computationally for operational models, which also makes observational-based prescriptions a convenient solution. Zhong et al. (2022) used relationships from an ensemble of aerosol models and satellite observations to identify the primary source of uncertainty in aerosol modelling results in biomass burning regions. Their study pointed out the incorrect simulations of lifetimes and the underestimation of mass extinction coefficients as the main reasons for their difficulty in matching observed aerosol optical depth (AOD). As the largest, time and device-consistent observational network, capable of constraining multiple aerosol intensive microphysical and optical properties, the AErosol RObotic NETwork (AERONET) has been used worldwide to constrain models and satellite algorithms (Omar et al., 2005; Li et al., 2010; Levy et al., 2010; Rosário et al., 2013; Russell et al., 2014; Chen et al., 2023). Chen et al. (2023) developed an aerosol optical module with observation-constrained Black Carbon properties to improve aerosol absorption simulation. Their sensitivity simulations show a reduction of 18 %–69 % in the biases of aerosol single-scattering co-albedo when compared with global observations from AERONET. Li et al. (2010) used AERONET retrievals to evaluate and improve the performance of a GCM aerosol optical module. They found their GCM to simulate flatter Aerosol Optical Depth (AOD) spectral dependence, indicating an Angstrom Exponent (AE) biased to low values, which suggests that the aerosol sizes simulated were too large. After adjusting the aerosol's size based on AERONET retrievals, the agreement between simulated and observed AOD improved for all aerosol regimes, but especially for smoke and dust scenarios. Rosário et al. (2013) used a set of spectral optical models developed from AERONET sky retrievals over distinct biomes combined with the concept of anisotropic areas of influence of the AERONET sites (Hoelzemann et al., 2009) to constrain smoke aerosol radiative effect modelling during South American biomass burning. By doing so, they were able to capture the effect of the regional variability of smoke optical properties (absorption and size-related) on the surface solar irradiance related to the biomes' distinct nature of smoke.

Global and regional cluster analysis of AERONET long-term retrievals of aerosol properties has proved valuable to classify observations in terms of aerosol optical regimes, providing means to qualitative constraints on aerosol properties (Omar et al., 2005; Levy et al., 2007; Russell et al., 2014; Li et al., 2019; Fan et al., 2021; Zhou et al., 2023). In these studies, the number of identified typical aerosol optical regimes varied from 4 to 10, numbers that were expected to likely represent either global or regional major aerosol scenarios, according to each study's focus. In their study, Zhou et al. (2023) found that regional aerosol regime classifications performed better than global classifications when applied to simulate AOD during pollution episodes and in different seasons in Beijing, China. They found larger differences between the strong and moderately absorbing aerosol regimes, namely dust and smoke regimes, when comparing global and regional clustering results. This is a consequence of the differences between China's regional dust and smoke aerosol particles' physical and chemical characteristics and those of global dust and smoke mean features. Another aspect highlighted by Zhou et al. (2023) is that smoke and dust-dominated optical regimes are more frequent globally than in China. Their result suggests that regional classification better captures typical aerosol optical regimes influencing a specific domain and, therefore, with the potential to improve observation-constrained simulations of aerosol radiative forcing.

Focusing on the Iberian Peninsula (IP), this study sought to characterize the typical aerosol optical regimes driving the variability of aerosol-intensive properties over the penin-

sula, aiming to constrain aerosol optical properties prescription in atmospheric models using a novel machine-learning approach. IP is a region affected by a highly dynamic and complex set of aerosols mixing, including natural and anthropogenic particles (Cachorro et al., 2016; Gómez-Amo et al., 2017). Natural sources include marine aerosols from the Atlantic Ocean and Mediterranean Sea, mineral dust from North Africa, and, eventually, wildfire emissions. Major anthropogenic sources are urban-industrial, particularly in more densely populated regions, and biomass burning driven by human activities, especially in the north and central Portugal and eastern and northern Spain. Regional column-integrated optical properties are highly sensitive to the mixing of this diversity of aerosol types, in particular to dust and smoke mixing (Gómez-Amo et al., 2017).

The manuscript is organized as follows: Sect. 2 includes a brief overview of the Iberian Peninsula, focusing on the main atmospheric circulation features and major aerosol particle sources affecting the region, followed by the description of the dataset and methods adopted to identify, characterize, and prescribe the identified aerosol typical regimes. Results and discussions are presented in Sect. 3. First, the identified aerosol optical regimes and their major features are described and contextualized. Subsequently, the results of the novel machine-learning approach to prescribing the optical regimes are discussed and evaluated. Finally, the main findings of our study are highlighted in the conclusion section.

2 Study region, data and methods

2.1 Study region

The Iberian Peninsula (Fig. 1), comprising Spain and Portugal, exhibits diverse climate conditions due to its complex topography and proximity to the Atlantic Ocean, the Mediterranean Sea, and North Africa. The wind circulation over the peninsula is shaped by its location between the Atlantic Ocean and the Mediterranean Sea, diverse topography, and interactions between regional and global atmospheric patterns, leading to complex wind circulations that significantly influence the region's climate. This results in distinct climate zones, from arid deserts to lush green forests. The Mediterranean climate spans most of Spain, including the eastern and southern coastal regions and central Portugal, featuring hot and dry summers, especially inland. Winters are mild, rarely dropping below 10 °C in coastal areas. Most precipitation, often rain, occurs in autumn and winter, leading to dry summers that increase wildfire risks. Wildfires regularly occur in the IP region, fueled by extreme weather conditions, abnormal high temperature records combined with strong, dry winds (Asfaw et al., 2022; Ermitão et al., 2023). Under these scenarios, the entire region can be affected by smoke plumes that often shape the entire region's optical properties (Elias et al., 2004; Gómez-Amo et al., 2017). But wildfires are more frequent in the north and central region of Portugal and the north and eastern portion of Spain (Ermitão et al., 2023; Alvarez et al., 2024). Oceanic climate is typical in northern coastal regions of Spain, such as Galicia, Asturias, and the Basque Country, and parts of northern Portugal. The Atlantic Ocean influences mild temperatures year-round, with minimal seasonal variation and abundant, evenly distributed rainfall. Annual precipitation can exceed 1000 mm, with frequent cloud cover and high humidity, especially in winter. The Continental climate of the central plateau (Meseta Central) and the Ebro Valley feature extreme temperature variations, with hot summers, highs often above 35 °C, and winters below freezing. The central regions have less precipitation than the coastal areas, with a semi-arid climate in some parts. Most rainfall occurs in spring and autumn. Arid and Semi-Arid Climates are found in Southeastern Spain, especially in Murcia and Almería, and parts of the Ebro Valley. These areas receive very low rainfall, often less than 300 mm annually, leading to desert-like conditions like those in the Tabernas Desert. Summers are extremely hot, while winters are mild. Southern Spain, especially the Andalusian region, can be affected by hot and dry winds from the Sahara, causing heat waves and dust storms.

The occurrence of Saharan dust events on the Iberian Peninsula usually peaks in March and June, with a marked minimum in April and lowest occurrence in winter according to Cachorro et al. (2016). Depending on the synoptic conditions and circulation patterns, dust transport can affect the entire peninsula (Toledano et al., 2007). The prevailing westerlies, blowing from west to east, are the dominant wind pattern over the Iberian Peninsula. These winds are most prominent in the mid-latitudes, including the Iberian Peninsula. More pronounced in the northern region during autumn and winter, these winds bring moist air from the Atlantic, increasing precipitation in Galicia, the Basque Country, and northern Portugal. While they also affect central and southern areas, their impact is moderated by the peninsula's topography and other wind systems. The northeast trade winds affect the southern and western coasts of Portugal and southwestern Spain, creating a mild and dry climate, especially in summer. In contrast, Mediterranean winds affect the eastern and southeastern coasts. Additionally, the Iberian Thermal Low, resulting from intense heating of the Iberian interior, creates a low-pressure area that draws air from the Atlantic and Mediterranean shores, leading to converging wind patterns. This circulation pattern enhances sea breeze penetration and moderates coastal temperatures. Southern Spain is influenced by the Sahara winds, as said, these dry winds often carry dust, increasing the temperature and reducing air quality. Calima is a type of wind that occurs when Saharan dust reaches the peninsula, especially in summer, causing hazy skies, a reddish tint, and low visibility. These winds are linked to high-pressure systems over North Africa and low-pressure systems over the western Mediterranean.

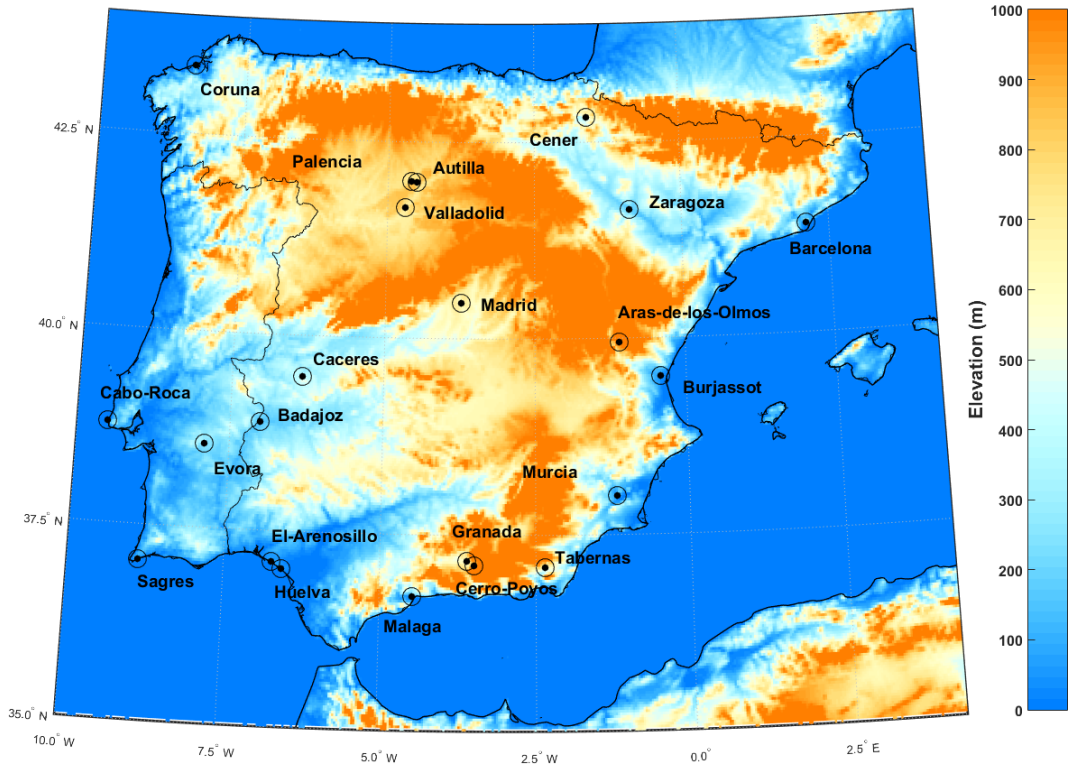

Figure 1. AERONET sites locations displayed on top of the Iberian Peninsula topography.

The wind circulation over the Iberian Peninsula is a dynamic and complex system shaped by global atmospheric patterns, regional geography, and local topography. The interaction of prevailing westerlies, trade winds, Mediterranean breezes, and local wind systems creates a diverse wind regime that affects the peninsula's climate. Understanding these patterns is essential for weather prediction, agriculture management, and tackling environmental challenges. According to Cachorro et al. (2016), these complex and contrasting influences of air masses from the Atlantic Ocean, Mediterranean Sea, European continent, and North Africa lead to a large spatio-temporal variability in aerosol properties, types, and mixing processes over the Iberian Peninsula. This makes the peninsula a challenging region for online modeling of aerosol microphysical properties and mixing state, therefore an interesting region to evaluate observation-based approaches, such as those based on climatological aerosol intensive optical properties from AERONET (Li et al., 2019; Fan et al., 2021; Zhou et al., 2023). The computation of optical properties for radiative transfer computations is usually based on a mass-weighted average of individual species at each grid point. This assumption of external mixing may not always be accurate, leading to significant uncertainties, such as excessive absorption by smoke aerosols and inaccuracies in dust size fractions. Observation-based approaches, such as those provided by AERONET retrieval climatology, attribute intensive optical properties to an effective aerosol based on actual observations. This method aims to reduce the uncertainties arising from the explicit simulation of these properties in climate models. The Iberian Peninsula, influenced by a variety of aerosol types, including dust, smoke, urban-industrial emissions, and marine aerosols, presents an interesting region to test this hypothesis.

2.2 AERONET aerosol inversion product

AERONET is a global ground-based network of sun photometers mainly aimed at characterizing columnar aerosol particle properties (Holben et al., 1998). From the direct Sun attenuation measurements, AERONET algorithms derive spectral Aerosol Optical Depth (AOD_λ) at the wavelengths 0.34, 0.38, 0.44, 0.50, 0.67, 0.87, 0.94, and 1.02 µm. The interval between direct sun measurements is typically 15 minutes, but only cloud-free conditions are considered for aerosol retrievals. From the spectral dependency of AOD at these wavelengths, AERONET provides Angstrom Exponent (AE), a parameter sensitive to the aerosol particle size distribution (Eck et al., 1999). AERONET also provides several other intensive properties that depend not on the amount but on the nature of the aerosol, related to particle size, shape, and composition, from sky radiance measurements up to nine times a day at the wavelengths 0.44, 0.67, 0.87, and 1.02 µm (Sinyuk et al., 2020). These intensive properties include microphysical parameters, such as refractive in-

dices ($n + ik$) and volume size distribution, and also optical parameters like Single Scattering Albedo (SSA), asymmetry parameter (ASY), Lidar Ratio (LR), Linear Depolarization Ratio (LDR), Angstrom Exponent, among others (Holben et al., 1998; Dubovik et al., 2002). This set of aerosol intensive properties is expected to capture most of the important aspects that differentiate the distinct aerosols' optical regimes that affect the study region. For instance, the imaginary part of the complex refractive index (k) and single scattering albedo (SSA) are properties that separate highly absorbing aerosol regimes from moderate and low absorbing regimes. Angstrom Exponent (AE) and Asymmetry Parameter (ASY) are properties that help separate aerosol regimes characterized by distinct size distributions. LR is highly sensitive to size and composition-related information, for instance, the real part of the complex refractive index. Meanwhile, LDR has high sensitivity to particle morphology, and it is widely used to separate dust particles from other aerosol types. Given the dependency of these intensive properties on the aerosol type (size and composition) and mixed state, it is possible to characterize the aerosol scenarios over a specific AERONET site in terms of their nature and sources (Eck et al., 1999; Dubovik et al., 2002). For instance, the LR is the ratio of the extinction coefficient to the backscatter coefficient and is crucial for identifying different aerosol types. It reflects how light scattering varies with particle size relative to the light wavelength. Small particles, like smoke, have a high LR, while large particles, like sea salt, have a low LR. Therefore, with a well-distributed regional network of AERONET's sun photometers, as that covering the Iberian Peninsula, one can characterize the spatial dynamics of aerosol types and mixture state influencing the regional aerosol regimes. Regarding the time period for the current study, it extends from 2003 to 2023. However, due to calibration and other operational aspects, some AERONET sites present different time ranges within this period.

Three key aspects of aerosol nature have been widely used to link aerosol regimes with particle emission sources. These aspects are absorption efficiency, size distribution, and shape (Dubovik et al., 2002). For instance, combustion-based sources, including biomass and fossil fuel burning, produce aerosol dominated by fine mode particles, and absorption ranges from moderate to strong, depending on the nature of biomass burning, fossil fuel, and ageing processes. In contrast, natural sources, such as deserts and marine environments, produce aerosols dominated by coarse-mode particles. Marine aerosol particles are characterized by very low absorption, while dust aerosol can exhibit high absorption, mainly in the UV and VIS bands (Smirnov et al., 2002; Dubovik et al., 2002). Furthermore, the irregular shape of dust particles is a key factor that differentiates them from other aerosol types. This distinctive feature is captured by AERONET retrievals of the LDR (Shin et al., 2018). Source attribution provides valuable insights into the typical intensive optical properties affecting the atmospheric column of a site resulting from complex aerosol state mixtures. This understanding is crucial as it addresses a major challenge that current aerosol modules in CMIP6 climate models face (Zhao et al., 2022). Reproducing climatological aerosol-intensive properties scenarios over specific regions has been a major goal of atmospheric models. In addition to evaluating aerosol modules in atmospheric models, AERONET's optical properties in typical regimes, which can be expressed as spectral aerosol optical models (Omar et al., 2005; Levy et al., 2007; Rosário et al., 2013; Zhou et al., 2023), are valuable for simulating aerosol direct radiative effects in environmental models (Rosário et al., 2013; Li et al., 2019). This approach is especially beneficial when high computational capacity is unavailable and explicit aerosol modules are not feasible.

With more than 25 years of operating a vast network of Cimel Electronique Sun–sky radiometers across the world, AERONET has provided highly accurate, ground-truth measurements of aerosol optical depth and other properties (Giles et al., 2019). It has been widely used as the main reference to evaluate and validate satellites (Gupta et al., 2018) and model products (Gliß et al., 2021). The two most critical intensive optical properties to estimating aerosol radiative forcing retrieved by AERONET, single scattering albedo (SSA) and asymmetry parameter (ASY), are related, respectively, to absorption and size of the aerosol. Their accuracies are aerosol loading dependent (Dubovik et al., 2002). For AOD > 0.4 at 440 nm (or > 0.2 at longer λ), SSA uncertainty $\approx \pm 0.03$, for lower AOD, uncertainty can be ± 0.05–0.07 or larger. Regarding ASY, uncertainty is about ± 0.02–0.05 when AOD is high (≥ 0.4 at 440 nm, ≥ 0.2 at longer wavelengths) but can be significantly larger at low AOD.

Aiming to identify a representative set of typical aerosol regimes that affect the Iberian Peninsula, we applied cluster analysis methods (described in Sect. 2.4) to the AERONET sky radiance retrievals dataset from 2003 to 2023, taking advantage of the extensive coverage of AERONET sites across the region. Within that period, a total of 4395 retrievals from AERONET Level 2.0 retrievals products were obtained and applied in the clustering process. Table 1 presents a set of intensive properties provided by AERONET that was used to identify typical aerosol scenarios in the Iberian Peninsula atmospheric column. The variables displayed cover all three previously mentioned aspects, absorption efficiency, size distribution, and shape, which are expected to characterize the distinct nature of aerosol types and mixture anticipated in the study region.

We selected only AERONET sites that operated for at least two years and that have sky radiance inversion available with the highest quality level 2.0. Some selected sites are still operational, while others have been discontinued. Figure 1 illustrates the geographical distribution of the chosen sites. Our selection encompasses various landscapes of the Iberian Peninsula, from coastal plains regions (Coruña, Sagres, Burjassot) to highland plateaus in the interior (Madrid, Val-

Table 1. List of AERONET inversions products (variables) used in clustering process followed by their abbreviation as defined by AERONET.

Variables	Abbreviation
Refractive index – real part	$RI_{Real}(440)$, $RI_{Real}(670)$, $RI_{Real}(870)$, $RI_{Real}(1020)$
Refractive index – imaginary part	$RI_{Imag}(440)$, $RI_{Imag}(670)$, $RI_{Imag}(870)$, $RI_{Imag}(1020)$
Single scattering albedo	SSA(440), SSA(670), SSA(870), SSA(1020)
Asymmetry parameter	ASY(440), ASY(670), ASY(870), ASY(1020)
Linear depolarization ratio	LDR(440), LDR(670), LDR(870), LDR(1020)
Lidar ratio	LR(440), LR(670), LR(870), LR(1020)
Fine and coarse modes volume median radius	VMR-F,VMR-C
Standard deviation from volume median radius, for fine and coarse modes	STD-F, STD-C
Fine and coarse modes effective radius	Reff-F, Reff-C

ladolid, Aras-de-los-Olmos) and lowland valleys (Zaragoza, Murcia). Regarding external air mass influence, sites in the southern border of IP are typically the first to experience the transport of dusty air masses from North Africa, with locations such as El-Arenosillo, Huelva, Malaga, and Sagres affected. The eastern sites (Barcelona, Burjassot, and Murcia) are expected to be strongly influenced by the Mediterranean air masses. Western and northern sites (Cabo da Roca, Coruna, Sagres) are directly under the influence of air mass from the Atlantic Ocean. Additionally, the Portuguese countryside (Evora) and eastern Spanish sites (Badajoz, Caceres) are located in regions that very often experience biomass burning during the dry season (Ermitão et al., 2023; Silva et al., 2023; Hammed et al., 2024; Alvarez et al., 2024).

2.3 Merra-2 aerosol diagnostic product

The MERRA-2 (Modern-Era Retrospective Analysis for Research and Applications, Version 2) Aerosol Diagnostic Product (ADP) is a comprehensive dataset provided by NASA that offers global information about atmospheric aerosols (Gelaro et al., 2017; Buchard et al., 2017). MERRA-2 combines observational data with numerical models (reanalysis project) to create a detailed long-term record of atmospheric dynamics and composition from 1980 to the present. Among other variables, the MERRA-2 ADP product offers a long-term view of aerosol mass distribution by types and the related optical properties (Buchard et al., 2017). Its extended temporal coverage allows analysis of aerosol trends, such as those related to changes in atmospheric composition due to human activity and the impact on climate. Key features of the MERRA-2 ADP include aerosol microphysical and optical properties such as optical depth, mass concentration, and size distribution. These properties are crucial for understanding aerosol loading and composition in the atmosphere and their role in the Earth's radiation budget and climate system. A key aspect of MERRA-2 APD for this study is that it provides aerosol-type column mass density, our target variable as a predictor of aerosol optical model regime. The MERRA-2 APD includes diagnostics for the aerosol types considered in most chemistry transport models: Dust (DT), Black-Carbon (BC), Organic Carbon (OC), Sea-Salt (SS), and Sulfate (SF). The aerosol-type diagnostics variables cover mass concentration at specific levels and are integrated into the entire atmospheric column, which are applied to estimate columnar optical properties, such as extinction, scattering, and absorption optical depths, at multiple wavelengths. For this study, the 550 nm wavelength was used as a reference. Optical properties are a function of aerosol species, particle size, and relative humidity. To convert from the simulated aerosol masses to optical quantities such as aerosol optical depth, MERRA-2 uses Optics look-up tables (LUTs) derived from Mie calculations using parameters from the Optical Properties of Aerosols and Clouds (OPAC; Hess et al., 1998), as described in Chin et al. (2002) and Colarco et al. (2010), except for dust-type aerosol, which is based on Colarco et al. (2014). Therefore, these optical properties are by-products of running the MERRA-2 reanalysis system and made available to the community via MERRA-2 ADP. Further details on this can be found in Buchard et al. (2017). From these extensive aerosol-driven optical properties, it is possible to derive several MERRA-2 ADP intensive optical properties, such as Single Scattering Albedo (SSA).

Given that the aerosol optical properties retrieved from each AERONET site are influenced by mixtures of different aerosol types, it is reasonable to assume that the impact of each aerosol type on the column's intensive optical properties is primarily determined by its concentration. Based on this premise, we propose a machine-learning approach that utilizes the aerosol-type column mass density predicted by chemistry transport models to prescribe the most accurate possible spatial distribution of the aerosol spectral optical model developed through cluster analysis of AERONET data. A description of the method presented in this study, exploring MERRA-2 products, can be found in Sect. 2.5.

2.4 Optical models development: cluster analysis

Cluster analysis has been extensively used to develop aerosol optical models based on AERONET sky inversion products (Omar et al., 2005; Levy et al., 2007; Russell et al., 2014).

The underlying principle is that AERONET instantaneous retrievals can be grouped into a certain number of clusters, each representing different categories of aerosol regimes. These studies have explored mainly the K-means clustering method, one of the most popular unsupervised machine learning algorithms for partitioning a dataset into a predefined number of clusters. However, specifying the number of clusters in advance poses a significant challenge for the K-means method. Fortunately, there are techniques available that reduce the subjectivity involved in this pre-definition. In our study, we adopted the Elbow method (Shi et al., 2021), a widely used method for determining the optimal number of clusters (k) in a K-Means clustering algorithm. It examines the relationship between a range of number of clusters and the Within-Cluster Sum of Squares (WCSS), which measures the variance within each cluster (Eq. 1)

$$\mathrm{WCSS} = \sum_{i=1}^{k} \sum_{x \in C_i} ||x - \mu_i||^2 \quad (1)$$

where k is the number of cluster C_i is the set of point in a cluster μ_i is the centroid of cluster i, and $|x - \mu_i|^2$ is the squared Euclidean distance. The WCSS measures the compactness of the clustering, and one wants it to be as small as possible. If clusters are tight and well-separated, WCSS will be small, because points are close to their centroids. If clusters are loose or overlapping, WCSS will be large. The Elbow method is based on a plot of WCSS (k) against the number of clusters (k). As k increases, WCSS always decreases; more clusters mean tighter groups. The goal of the method is to identify the point (k) where the rate of decrease in WCSS sharply slows down, indicating that adding more clusters yields diminishing returns. We ran our clustering algorithm with k varying from 2 to 10 clusters. For each k, we calculated the total WCSS. The k results against WCSS were displayed in a plot, and the optimal number of clusters was defined based on the location (k) of the bend (elbow) in the plot from which the change in WCSS slows down. This bend in the curve indicates the point where adding more clusters no longer gives meaningful improvement.

The Elbow method has been widely used because of its straightforward approach to estimating the most appropriate number of clusters. However, we recognize that it still carries a certain degree of subjectivity, as it relies on visual interpretation. To reduce this subjectivity, we combined the Elbow and Stability methods to evaluate the optimal number of clusters that best represent the major aerosol regimes affecting the study region. Although more rigorous methods are available in the literature, defining the number of clusters remains a challenge, and different approaches often lead to distinct solutions (Krishnaveni et al., 2023). Nevertheless, despite the limitations of the Elbow method, the number of clusters identified in our study seems to provide a coherent characterization of optical regimes affecting the Iberian Peninsula.

The K-means clustering analysis was performed using Scikit-learn, a Python open source machine learning library that supports supervised and unsupervised learning (Abraham et al., 2014). All our analyses were performed using the Scientific PYthon Development EnviRonment (Spyder), an open-source IDE for the Python language. As part of the preprocessing step, the values of the features listed in Table 1 were normalized using the *StandardScaler*( ) utility from *sklearn.preprocessing* package, which computes the mean and standard deviation. Then the scaled dataset was obtained subsequently by subtracting all values of the features from their respective mean and normalized by the corresponding standard deviation. With this scaling process we expected to avoid the dominance of features with large numeric ranges.

To evaluate the robustness of the clustering results, a set of sensitivity analysis using the Scikit-learn library was performed. These tests were meant to test numerical stability, sampling robustness, clusters reproducibility, separation quality and presence of transitional regimes. A summary with all the results of these performed tests can be seen in the Supplement. First, a jitter robustness test was conducted by adding Gaussian noises taking different uncertainty estimates (5 %, 10 %, 20 %) to the standardized feature matrix and rerunning the clustering algorithm multiple times (200 runs). The resulting partitions were compared with the original clustering using the Adjusted Rand Index (ARI), which assesses the sensitivity of the clustering structure to perturbations in feature space (mimicking features uncertainties). Second, a bootstrap robustness analysis was implemented by repeatedly resampling the dataset with replacement and recomputing the clustering solution for each resampled dataset. The ARI between the original and bootstrap-derived clusterings was calculated to evaluate the dependence of the clustering structure on specific samples and to test its reproducibility under data variability. In general, the mean ARI results for both jitter and bootstrap robustness analysis (Table S3) presented values above 0.80, which indicate high similarity between the originally predicted clusters and the perturbed, which support the clustering structure robustness to random noises.

Cluster-level stability was quantified using a cluster retention score, defined as the average probability that members of an original cluster remain grouped together across perturbation runs also applying gaussian noises references (5 %, 10 %, 20 %) to the standardized feature matrix and rerunning the clustering algorithm multiple times (200 runs). This metric allows identification of highly stable regimes as well as potentially transitional or mixed clusters. With most of the cluster retention scores above 0.95 (Table S4), results show that the obtained cluster regimes are highly stable. The exception is cluster 3, which presented a retention score of 0.88, which can be considered stable but somewhat overlapping. Finally, a consensus (co-assignment) matrix was constructed by computing, for every pair of samples, the pro-

portion of runs in which the two samples were assigned to the same cluster. From this matrix, mean intra-cluster and inter-cluster co-assignment probabilities were derived to quantify internal cohesion and external separation (Table S5 in the supplement). The results of high intra-cluster probability (> 0.85) and low inter-cluster probability (< 0.10) show that in general members of the same cluster are consistently grouped together, which corroborates the quality of the clustering results. This test was also conducted by adding gaussian noises considering different uncertainty estimates (5 %, 10 %, 20 %).

Together, these diagnostics provide a comprehensive evaluation of clustering stability, reproducibility, and structural robustness.

2.5 Optical models spatial prescription: random forest technique

Once the optimal number of clusters is defined, which corresponds to the expected number of major optical properties regimes to influence the study region, and the clustering process is performed, each cluster is characterized by a set of AERONET instantaneous retrievals of optical and microphysical properties that are expected to express an optical property regime. Also, each AERONET instantaneous retrieval is tagged with the cluster number that it belongs to. By averaging the instantaneous properties of each cluster, we set the reference values that represent the mentioned major aerosol optical properties regimes.

We propose a machine-learning approach that utilizes the well-known random forests supervised algorithm (Breiman, 2001) to spatially represent the aerosol optical models defined by the cluster analysis for each AERONET site (described in Sect. 2.4). The implemented method was tested using exclusively aerosol column mass density fields from MERRA-2 (Table 2) to establish the spatial distribution of the optical regime defined by the cluster's average. This approach is also suitable for chemistry transport models.

MERRA-2 time series of column mass density for each aerosol type (DT, BC, OC, SS, SF) over each AERONET site were collocated with the network inversion products used to derive the clusters representing the distinct aerosol regimes over the Iberian Peninsula (described in Sect. 2.4). Only MERRA-2 column mass density fields were used in the Random Forest training process; optical properties fields from the reanalysis system were not used at this stage. Merra-2 column mass densities are available with a frequency of 1 h, while AERONET optical properties instantaneous retrievals are provided at irregular times, due to its dependence on cloud cover and AOD criteria (AOD at 440 nm > 0.4). So, for each AERONET retrieval, our script searches for the MERRA-2 closest hour to synchronize the two datasets. Therefore, the collocation between AERONET retrievals and MERRA-2, for a spatial matching we considered the nearest neighbor by taking the MERRA-2 grid cell that contains the AERONET station location, and for temporal collocation MERRA-2 hourly aerosol diagnostics were matched to the closest AERONET observation time. Each AERONET instantaneous aerosol microphysical and optical properties inversion retrieval (Sinyuk et al., 2020) was connected to the corresponding cluster to which it belongs. Likewise, as mentioned, each instantaneous aerosol microphysical and optical properties inversion retrieval was also connected to the closest in-time combination of MERRA-2 data of aerosol-type column mass density (DT, BC, OC, SS, SF). With this, we built a time series of 4309 points of spatial and temporal collocated MERRA-2 aerosol types of column mass density with the developed clusters occurrences over each AERONET site, which was used in a training process aiming to predict the suitable cluster given a specific combination of aerosol types column mass density predicted by MERRA-2. This time series was randomly divided into training and testing subsets, with 70 % (3016 collocated combinations) of the data used for model training and 30 % (1293 collocated combinations) reserved for independent evaluation. This was done using the train_test_split utility from the Scikit-learn library (Abraham et al., 2014).

The algorithm uses training data to learn the relationship between the combination of aerosol-types' columnar mass density and the target, which are the previously developed clusters from AERONET aerosol-intensive properties. The training was done using the Random Forest Classification algorithm (RandomForestClassifier) from Scikit-Learn.

We used stratified k-fold cross-validation integrated within a RandomizedSearchCV hyperparameter optimization process as a strategy. Our hyperparameter optimization was performed using RandomizedSearchCV with five-fold cross-validation. The search space included the number of trees (n_estimators) sampled uniformly between 50 and 500 and the maximum tree depth (max_depth) sampled between 1 and 20. A total of five random hyperparameter combinations were evaluated, and the best-performing model was refitted on the full training dataset. The random search methodology was used to find parameter combinations inside the parameter space without the processing demands of grid search and with the stratified k-fold cross-validation we search to ensure that each fold has approximately the same class proportions as the full dataset, which allows a fair evaluation, since every validation set includes samples from all classes. This also contributes to the meaning of the performance metrics in relation to the minority classes, for example strong absorbing aerosol regimes. The stratified k-fold also favours a more stable training, given that in every training split the less frequent aerosol property regimes are also seen, which helps to reduce variance in model performance across folds. This strategy contributes to improving the hyperparameter tuning, once the RandomizedSearchCV won't select parameters based on misleading folds. So, by preserving class distribution in every fold and preventing biased results, the strategy based on stratified k-fold cross-validation

Table 2. Predictor variables from Merra-2 (aerosol-type column mass density) used in the machine learning process to prescribe the aerosol optical regime (optical model).

Variables	Abbreviation	Unity	Spatial resolution
Dust column mass density	DUCMASS	$kg\,m^{-2}$	$0.5° \times 0.625°$
Black carbon column mass density	BCCMASS	$kg\,m^{-2}$	$0.5° \times 0.625°$
Organic carbon column mass density	OCCMASS	$kg\,m^{-2}$	$0.5° \times 0.625°$
SO_2 column mass density	SO2CMASS	$kg\,m^{-2}$	$0.5° \times 0.625°$
SO_4 column mass density	SO4CMASS	$kg\,m^{-2}$	$0.5° \times 0.625°$
Sea salt column mass density	SSCMASS	$kg\,m^{-2}$	$0.5° \times 0.625°$

helps to handle class imbalance, which in turn improves the model reliability and generalization. Class imbalance is typical in atmospheric aerosol characterization, where extreme but radiatively important aerosol regimes, like intense smoke episodes, are rare compared to more common background conditions. Therefore, with the strategy described, we also aimed to address the issues of class imbalance of aerosol regime classification in our study.

Cross-validated performance indicators were used to select the final configuration in order to reduce overfitting and ensure consistent performance across aerosol regimes. To evaluate model performance across aerosol regimes, and not to rely only on the overall accuracy, the performance metrics were computed individually for each regime

The confusion matrix utility from the Scikit-learn library (confusion_matrix) was used to visualize the performance of the models by comparing true labels with predicted labels. It allowed us to evaluate performance for each class individually and to support the interpretation of the per-class metrics calculated, namely Accuracy, Precision and Recall, and F_1 score. While the confusion matrix provides the context that explains the model performance, the per-class metrics provide numerical performance values for each class.

Accuracy represents the number of correctly classified data instances over the total; it checks the predictions against the actual values in the test set and returns the percentage of times the model got right. Precision and recall are two critical metrics for evaluating the performance of a classification model. Precision is the proportion of true positives among all the predicted positive cases (true and false), meaning it measures the accuracy of positive predictions (Eq. 2). Recall is the proportion of true positives among all actual positive cases (true and false), meaning it measures the model's ability to identify positive cases (Eq. 3). The F_1 score, the harmonic mean of a model's precision and recall, takes both precision and recall and provides a more balanced measure of a model's performance (Eq. 4). The F_1 score is set to be a value between 0 and 1, indicating, respectively, poor precision and recall and high precision and recall, which is ideal.

$$\text{Precision} = \frac{\text{True positive}}{(\text{True positive} + \text{False positive})} \tag{2}$$

$$\text{Recall} = \frac{\text{True positive}}{(\text{True positive} + \text{False negative})} \tag{3}$$

$$F_1 = \frac{2 \times (\text{Precision} \times \text{Recall})}{(\text{Recall} + \text{Precision})} \tag{4}$$

To identify which aerosol types most influence aerosol regime prescription and to understand whether meaningful types are driving predictions, we used the best_rfc.feature_importances_, an utility in scikit-learn's RandomForestClassifier, to calculate the scores indicating the importance of each aerosol types in the training dataset. The importance of an aerosol type in making predictions was based on how much it reduces impurity across all trees. Each decision tree in the forest splits data using different features, and each split reduces impurity. The reduction in impurity is attributed to the feature used at that split. An aerosol type importance is based on the frequency that it is used to split nodes.

3 Results

The results section is divided into three subsections. The first one presents the results of identifying the typical aerosol optical regimes affecting the Iberian Peninsula using cluster analysis. The second subsection discusses the results and the performance of spatial prescription of these typical aerosol regimes by applying machine learning (Random Forest) to the columnar density of MERRA-2 aerosol components. Finally, case studies applying the method developed are presented and discussed.

3.1 Cluster analysis: optical models development

The number of clusters (k) selected to characterize the typical optical aerosol regimes over the Iberian Peninsula was defined based on the Elbow method (Fig. 2), which indicated five clusters were the optimal number to capture the aerosol regime variability. We also evaluated from the Elbow

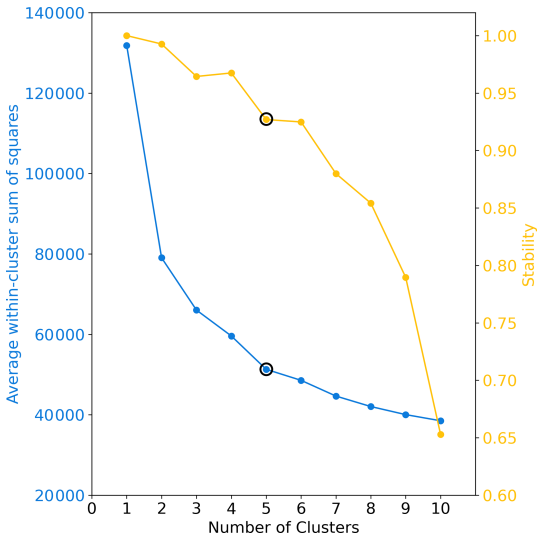

Figure 2. Average of sum of squares within-cluster and cluster stability as function of the number of clusters.

method that there is a sharp bending at $k = 2$, which we associated with a clustering separation between aerosol regimes strongly dominated by coarse mode, dust regimes, and regimes dominated by fine mode, non-dust regimes. However, to cover more specific regimes within these two macro-regimes (dust regimes vs. non-dust regimes), a higher k is required, and $k = 5$ is revealed to be the second sharpest bending. Cluster stability as a function of the number of clusters was also evaluated as a way of evaluating whether the clusters obtained are meaningful and not just artifacts of randomness or noise. High stability suggests clusters represent real structure in the data, not just random fluctuations. The stability for $k = 5$ is above the 90 % threshold, similar to $k = 6$, a number after which stability sharply decreases. Therefore, combining the Elbow method and stability reinforced $k = 5$ as an optimal cluster number to capture the typical aerosol scenarios over the Iberian Peninsula, reducing the subjectivity usually associated with the K-means clustering method.

We applied the cluster analysis once we defined the optimal number of clusters. As described, the result for clustering process robustness was assessed using the fraction of points changing cluster membership relative to the original classification by perturbing the input data by ± 1 SD (standard deviation) and rerun the K-means clustering. The fraction of points changing cluster assignment was 15.3 % for the $+1$ SD perturbation and 17.6 % for the -1 SD perturbation, yielding a mean sensitivity of 16.5 %. Only 0.5 % of points changed cluster membership under both perturbations, indicating that the observed sensitivity is largely confined to boundary points, while the cluster cores remain robust.

Figure 3 presents a combination of graphics used for aerosol properties analysis, highlighting the obtained clusters' behavior and distinction. The first graphic (Fig. 3a) represents the Aerosol Optical Depth (AOD) as a function of Angstrom Exponent (AE), which allows us to relate aerosol loading variability with aerosol regimes dominated either by coarse or fine mode (Eck et al., 1999). This analysis shows that two of the clusters (C0 and C1) are regimes dominated by coarse mode particles (AE < 1.0), while the remaining three (C2, C3, and C4) are regimes under the stronger influence of fine mode particles (AE > 1.0). The second plot displays the asymmetric parameter against the single scattering albedo at 440 nm. This plot aims to elucidate the clusters' distinctions related to particle absorption efficiency and the asymmetry between hemispherical forward and backward scattering. Aerosol regimes dominated by coarse particles tend to exhibit more significant forward scattering and, consequently, higher asymmetry parameter values. In contrast, lower asymmetry parameter values are expected in fine mode regimes (Eck et al., 1999; Dubovik et al., 2002). This pattern is evident in the graphic; clusters C0 and C1 present higher asymmetry parameter values. It is also possible to identify the distinction between the non-dust regimes C2, C3, and C4. C2 presents the lowest asymmetry parameter values, while it is the most absorbing of the clusters, according to its single scattering albedo values. Small and highly absorbing particles are commonly associated with urban pollution or fresh smoke plumes from biomass burning (Dubovik et al., 2002; Omar et al., 2005; Levy et al., 2010; Martins et al., 2009). The C3 cluster differs significantly from C2 by presenting higher asymmetry parameter values, an indication of a shift to larger particle sizes. C3 has higher single-scattering albedo values, indicating a less absorbing aerosol regime. SSA alone did not help to differentiate the two clusters dominated by coarse mode particles (C0 and C1). C0 asymmetry parameter values tend to be lower than those of C1, suggesting that the former could be a dusty mixture not as close to a pure dust scenario as C1. The traditional plot of Lidar Ratio (LR) against Linear Depolarization Ratio (LDR) (Kanitz et al., 2013; Illingworth et al., 2015) confirms this hypothesis (Fig. 3d). Pure dust regimes of aerosol, due to their high level of non-spherical particles, produce higher LDR (Groß et al., 2011). The C1 cluster presents higher values of LDR than C0, indicating that C1 is closer to a pure dust regime. The C0, while a dust regime, is likely to represent a mixed scenario given its LDR values consistent with dust and smoke mixing (Kanitz et al., 2013). LDR values below 15 %, which is the case of the clusters C2, C3, and C4, are typically associated with fresh/aged smoke, urban-industrial pollution, and marine particles scenarios. The analysis of the real part versus the imaginary part of the complex refractive index (Fig. 3c) emphasizes C2 as the aerosol regime with the largest absorption and highlights that the real part of the complex refractive index is the main aspect differentiating C3 and C4.

Figures 4 and 5 present the clusters averages for selected features: size distribution, complex refractive index, single scattering albedo, and asymmetry parameter. A more detailed

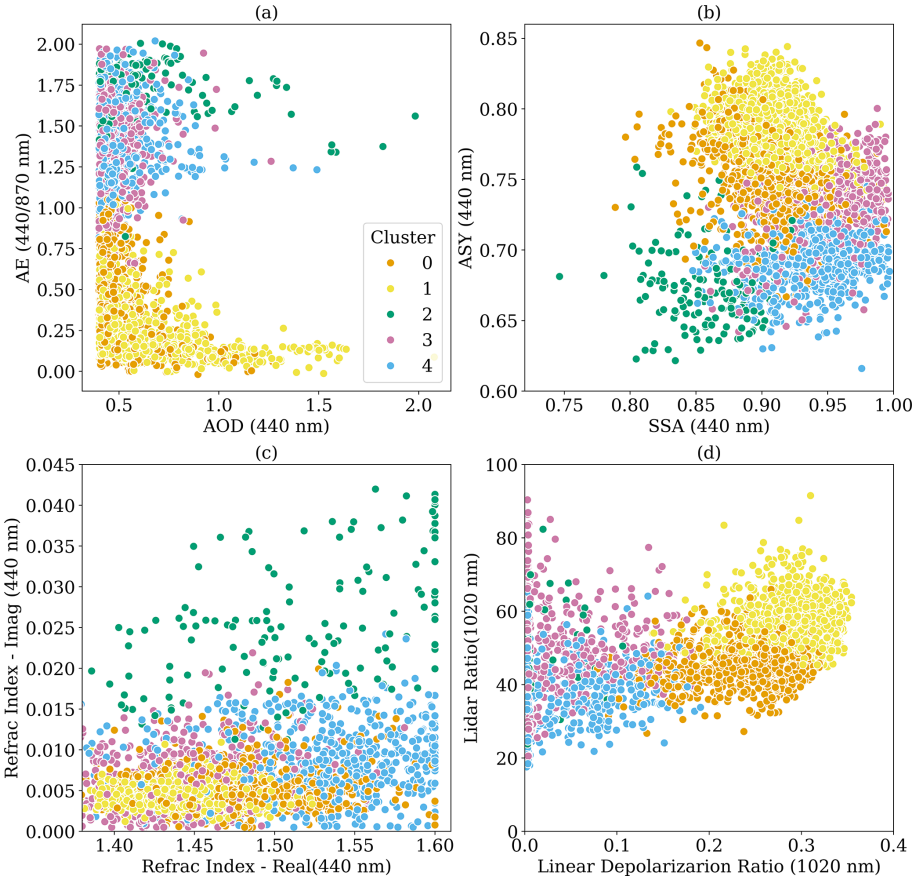

Figure 3. Scatterplot of the clusters elements as function of different parameters: **(a)** extinction Angstrom Exponent (AE) as function of Aerosol Optical Depth (AOD) at 440 nm; **(b)** Asymmetry Parameter (ASY) as function of Single Scattering Albedo (SSA) at 440 nm; **(c)** Lidar Ratio as a function of Linear Depolarization Ratio at 1020 nm; **(d)** refractive index at 440 nm: imaginary part as function of Real part.

summary of the mean behavior of the clusters is presented in Table 3. The average size distribution of the clusters confirms that aerosol regimes affecting the Iberian Peninsula vary between two scenarios dominated by coarse mode (C0, C1), named here as dust regimes, and three scenarios when coarse mode is not dominant, here considered as non-dust regimes. There are differences between the dust regimes: C1 is associated with a higher coarse particle loading than C0. Among the non-dust regimes (C2, C3, and C4), the main difference is seen between C2 and the other two. C2 is characterized by a larger fine particle loading. Between C3 and C4, one can observe a larger radius spread for C3 regarding the contribution of the fine mode, which indicates a potential growth of particles via processes such as water uptake, aging, and coagulation, or that the aerosol regime mixture includes sources that naturally produce slightly larger fine particles. These features usually indicate more aged, more hygroscopic, or more humidified aerosol compared to freshly emitted, dry fine particles.

Clusters C2 and C4 have close values for the real part of the refractive index, but cluster C2 has a much larger imaginary part, justifying its lowest SSA (Fig. 5). The C2 strong absorption combined with its smaller particles suggests that it is likely associated with fresh smoke (Reid and Hobbs, 1998; Reid et al., 2005). The average of the real part of the complex refractive index corroborates the difference between the C3 and C4 aerosol regimes. According to Moise et al. (2015), a variation as such observed between C3 and C4 (1.4 to 1.5) could produce an increment of 12 % in estimating the direct aerosol radiative forcing over the solar spectrum wavelength range. Zhao et al. (2019) also showed that the direct aerosol radiative forcing is estimated to vary by 40 % when the real part of the complex index values varies between 1.36 and 1.56. The reasons for the differences observed between the real parts of C3 and C4 remain unclear. However, the spatial distribution of the clusters (see Fig. 6) indicates that C3 is more prevalent in the eastern region of the Iberian Peninsula, which is the wettest area and more exposed to air masses from the Mediterranean and Eastern Europe. Additionally, the low values of the real part of the complex refractive index for C3 align with aerosol regimes that have a strong contribution from sulfate particles. The spectral

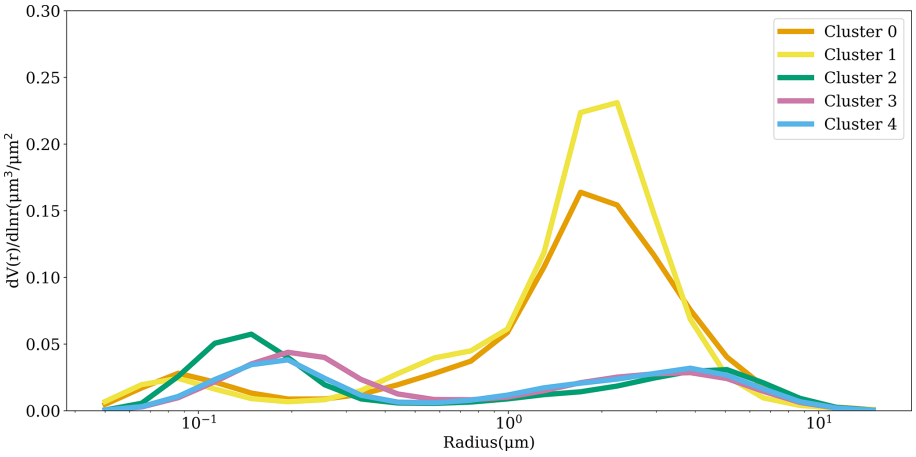

Figure 4. Clusters mean volume particle size distribution as a function of radius. These size distributions correspond to the average of the instantaneous size distributions retrieved by AERONET from each identified cluster. The numeric values of each cluster size distribution can be found in Table S2.

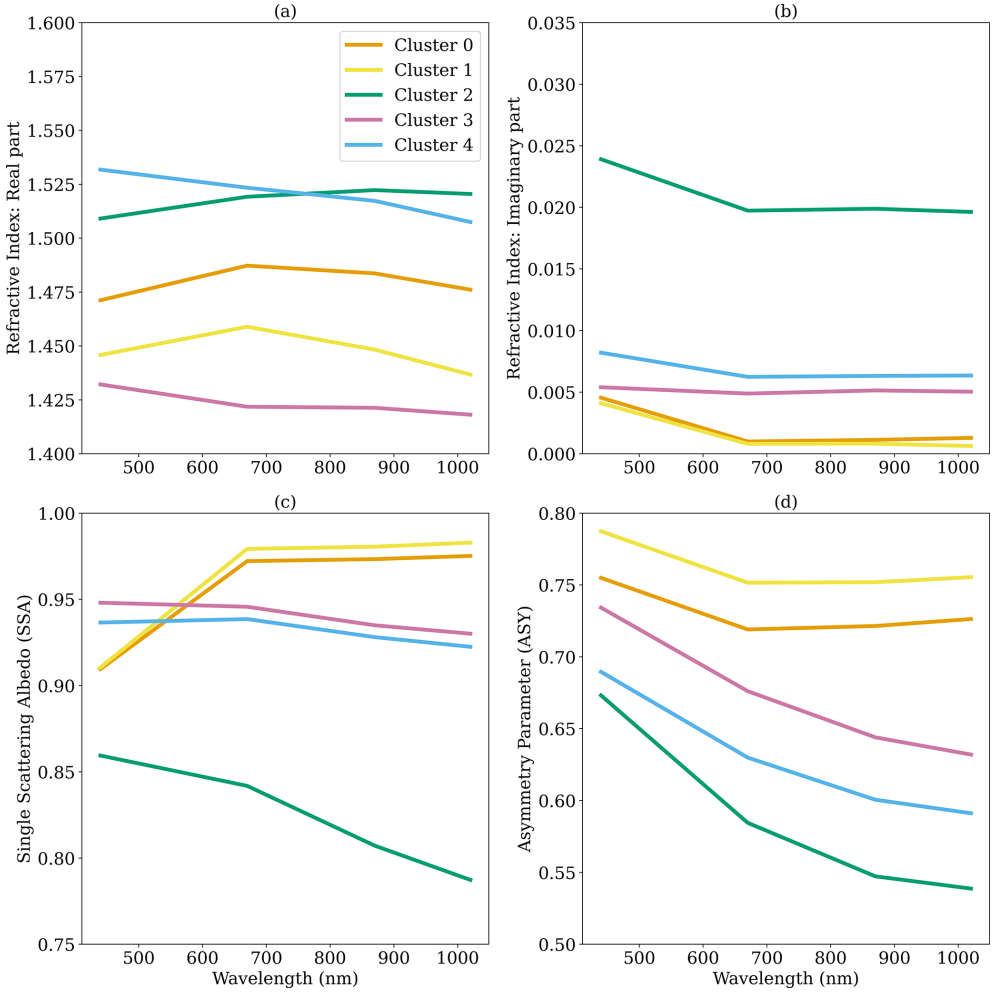

Figure 5. Clusters average of complex refractive index, **(a)** real and **(b)** imaginary parts, **(c)** single scattering albedo and **(d)** asymmetry parameter.

Table 3. Summary of the clusters based on the average of optical and microphysical properties. A detailed description of the clusters can be found in Tables S1 and S2. The values in the brackets correspond to standard deviation.

Properties	Cluster0 (polluted dust)	Cluster1 (pure dust)	Cluster2 (strongly absorbing smoke)	Cluster3 (Urban-industrial pollution)	Cluster4 (moderately absorbing smoke)
Number of records	1308	1665	153	660	609
Percentage (%)	29.76	37.88	3.48	15.01	13.74
Ref_Idx_Real (440 nm)	1.47 (0.04)	1.44 (0.03)	1.51 (0.07)	1.43 (0.06)	1.52 (0.05)
Ref_Idx_Img (440 nm)	0.005 (0.002)	0.004 (0.001)	0.025 (0.009)	0.006 (0.004)	0.009 (0.004)
VMR-F	0.14 (0.03)	0.14 (0.03)	0.16 (0.02)	0.21 (0.04)	0.18 (0.04)
STD-F	0.61 (0.09)	0.67 (0.07)	0.42 (0.06)	0.47 (0.06)	0.41 (0.05)
REff-F	0.12 (0.02)	0.12 (0.02)	0.14 (0.02)	0.18 (0.03)	0.17 (0.03)
REff-C	1.68 (0.16)	1.61 (0.13)	2.44 (0.43)	2.31 (0.38)	2.25 (0.49)
VMR-C	2.02 (0.23)	1.88 (0.17)	3.10 (0.45)	2.82 (0.42)	2.82 (0.57)
STD-C	0.60 (0.52)	0.54 (0.04)	0.68 (0.06)	0.63 (0.05)	0.67 (0.05)
AOD (440 nm)	0.50 (0.11)	0.58 (0.21)	0.64 (0.29)	0.48 (0.09)	0.51 (0.13)
SSA (440 nm)	0.91 (0.03)	0.91 (0.02)	0.86 (0.03)	0.95 (0.03)	0.94 (0.03)
ASY (440 nm)	0.76 (0.02)	0.79 (0.19)	0.67 (0.03)	0.73 (0.03)	0.69 (0.02)
AE (440/870 nm)	0.40 (0.25)	0.24 (0.14)	1.67 (0.20)	1.43 (0.26)	1.47 (0.25)
LR (1020 nm)	64 (9)	70 (8)	89 (16)	77 (17)	61 (15)
LDPR (440 nm)	0.17 (0.04)	0.21 (0.04)	0.01 (0.03)	0.03 (0.04)	0.03 (0.05)

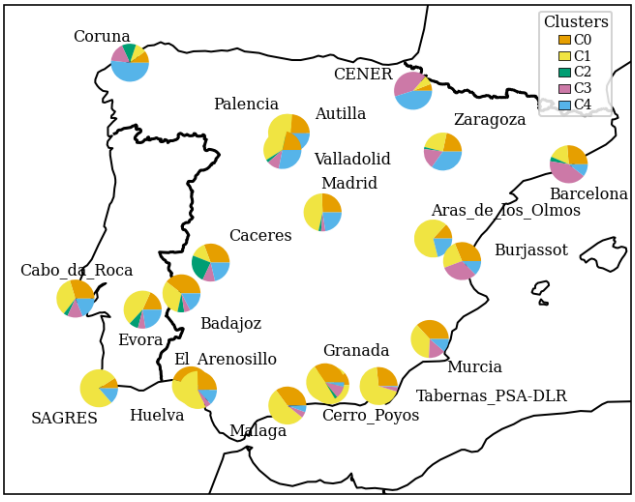

Figure 6. Proportions of the occurrence of the clusters of aerosol regimes at the AERONET sites across the Iberian Peninsula.

dependency of the single scattering albedo corroborates our attribution of the C0 and C1 to a dust regime. Dust particles are characterized by strong absorption in the UV spectrum (Dubovik et al., 2002), which decreases as the wavelength increases, a feature present in both C0 and C1. Also, consistent with dust-dominated regimes, C0 and C1 have the largest mean asymmetry parameters at all wavelengths.

The analysis above and the summary provided by Table 3 provide several specific characteristics that help us to contextualize the clusters. To enhance this understanding, we add the spatial (Fig. 6) and seasonal (Fig. 7) distribution of the clusters into our analysis. C0 and C1 aerosol regimes are dominated by dust, where C1 is the closest regime to what we could call a pure dust scenario. Both aerosol regimes, C0 and C1, affect practically the entire Peninsula (Fig. 6) and all year round, but it is more frequent in the southern part of the Peninsula, an expected feature considering that the dust particles are mainly transported from North Africa (Cachorro et al., 2016; Gómez-Amo et al., 2017). The C2 cluster is the most absorbing regime and is characterized by the smallest fine mode particles (Table 3). Its spatial distribution (Fig. 6), with more frequent occurrence along the belt spanning from Evora, in Portugal, to Caceres, in Spain, a region known for high recurrence of biomass burning, reinforces our hypothesis. Additionally, the seasonal distribution of C2 in this region coincides with the peak of the biomass burning season. The C3 aerosol regime also occurs over all AERONET sites throughout the year, but it is dominant in the eastern and northeastern portions of the Iberian Peninsula. Among non-dust regimes, its unique feature is its very low real part of the refractive index. C4, as C3, is weakly absorbing according to its single scattering albedo. C4 is present across the entire Peninsula, but its occurrence increases in the central and northern portions, which are more prone to biomass burning. An important feature of C4 is that its occurrence increases during the summer and the beginning of autumn (Fig. 7) in the central region of the Iberian Peninsula, from Évora (Portugal) to Madrid (Spain), when the region's biomass burning season is underway. These aspects led us to hypothesize that

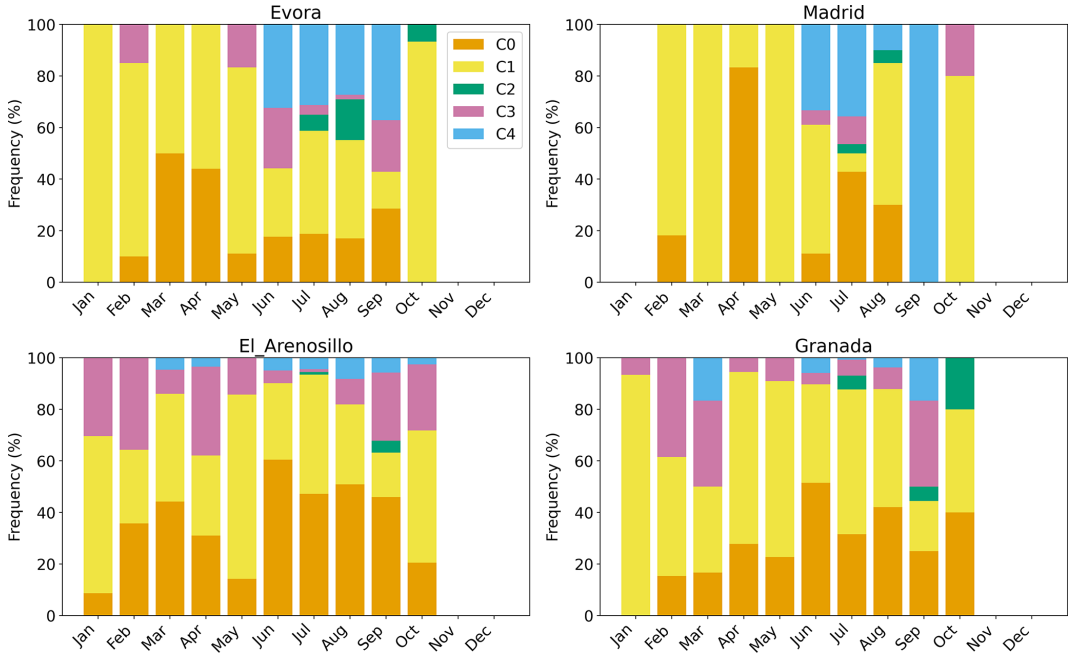

Figure 7. Clusters relative monthly occurrence over the AERONET sites representatives of the Iberian Peninsula western lowlands (Evora), highlands plateau (Madrid) and southeast lowlands (El Arenosillo, Granada).

C4 is an aerosol regime under the strong influence of smoke aerosol particles.

Figures 7 and 8 provide a perspective view on the seasonal occurrence of each cluster based on sites that represent different regions of the Iberian Peninsula.

3.2 Random Forest classifier: performance and optical models spatial dynamic

The Random Forest training of MERRA-2 aerosol-type column mass density as predictors of aerosol optical regime covered 70 % of the AERONET sky inversions used in this study, combining datasets from all sites. The testing dataset, constituted by the remaining 30 %, was used to evaluate the model's performance. The best parameters obtained from the optimization using RandomizedSearchCV were the number of decision trees of 477 (n_estimators = 477) and the maximum depth of trees of 19 (max_depth = 19). There are several metrics for assessing machine learning performance. Figure 9 presents the one used in this study, the Normalized Confusion Matrix (NCM), which expresses the percentage of correct and incorrect predictions (where the classifier got confused). In the matrix, the rows represent the true labels, and the columns represent the predicted ones. The values along the diagonal indicate the percentage of times where the predicted matches the true label. The other cells reflect instances where the classifier mislabeled an observation; the column tells us what the classifier predicted, and the row tells us the correct label.

For all clusters, the classifier's correct predictions surpassed the incorrect predictions, with a maximum frequency of correct predictions close to 80 % obtained for C1. The minimum percentage of correct prediction, about 60 %, was obtained for C2, the highest absorbing cluster. Regarding dust regime clusters, despite the struggle to predict C0, it is possible to see that, in this case, the classifier's main confusion is with the C1, which is also a cluster related to an aerosol scenario dominated by coarse mode particles (dust regime), as with C0. The classifier's confusion in this case is between the two dust-regime models; therefore, the induced error in optical properties prescription would be lower than that if the confusion was between a dust and a non-dust regime, especially like C2, which is substantially different from any of the dust regimes. Rarely does the classifier take either C0 or C1 as C2, C3, and C4, a case where substantial error in the optical properties prescription would be expected. By combining C0 and C1 results in the NCM, the percentage of correct predictions achieved by the classifier indicating dust regime is higher than 95 %. Similarly, the classifier rarely takes C3 and C4 as C0, C1, and C2. Given that C3 and C4 are also close in terms of their optical properties, especially concerning absorption, some degree of confusion among them is expected. Nevertheless, these aspects of the confusion matrix among close clusters are important to identify where the model needs extra training, for instance, considering longer time series when available and adding new and relevant predictors, such as Brown Carbon, an important aerosol component not available in the current MERRA-2

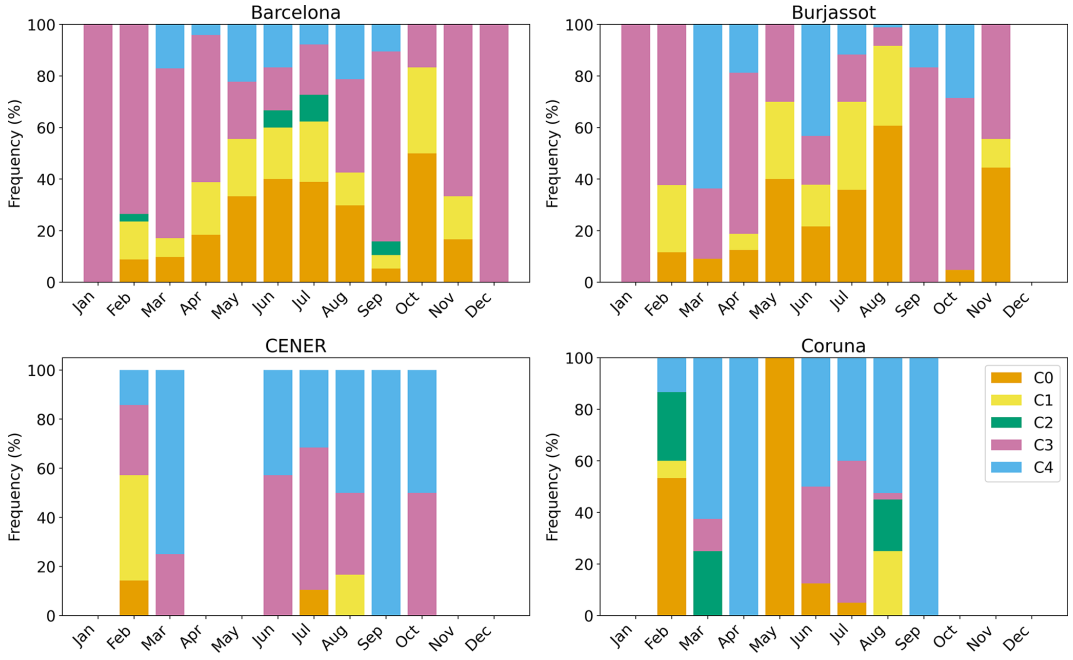

Figure 8. Clusters relative monthly occurrence over the AERONET sites representatives of the following Iberian Peninsula regions: Eastern Coast (Barcelona, Burjassot) and Northern (Coruna, CENER).

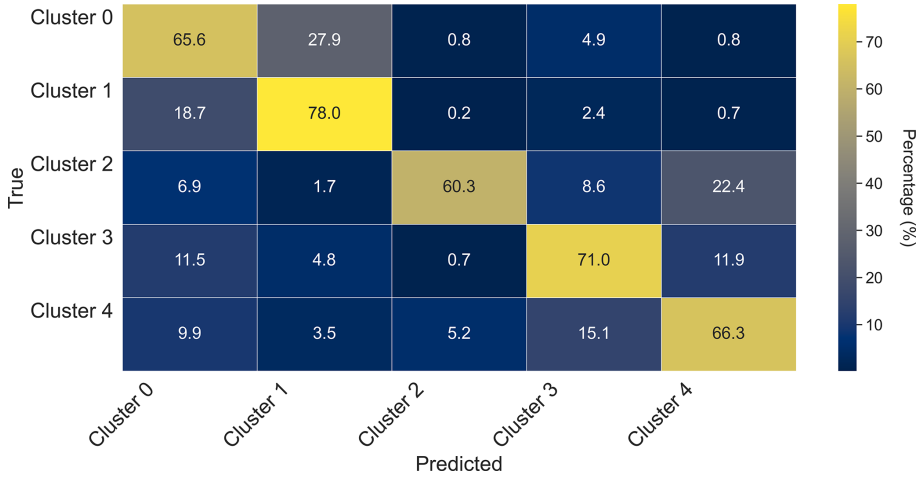

Figure 9. Normalized confusion matrix of the Random Forest classifier applied to the prediction of the clusters that describe the typical aerosol optical regime based on MERRA-2 aerosol components column mass density.

aerosol reanalysis products. C2, the least frequent and the one representing the most absorbing aerosol regime over the Iberian Peninsula, is rarely mislabeled as C0 or C1, but often mislabeled as C3 or C4. Still, the score percentage is around 60 %.

To provide further insight into the model performance, we also examined other metrics commonly used to evaluate Random Forest training. Precision, Recall, and F_1 score were calculated for both scenarios, the trained model applied to the test and to the train dataset (Table 4). The results indicate that the model generalizes well, without significant overfitting. Even for Cluster 2, which has a small number of occurrences, the model was able to maintain high precision and score. The general accuracy did not drop critically for the test data (0.70) when compared with the train dataset (0.88), another indicator of the model's ability to generalize. The trained model applied to the test dataset achieved a general accuracy of 70 %, meaning it correctly predicted the aerosol regime in three out of four cases. For all clusters, all metrics adopted were higher than 0.60, with precision and recall values exceeding 0.75 in some cases. The precision metric indicates how often the positive predictions are correct. The

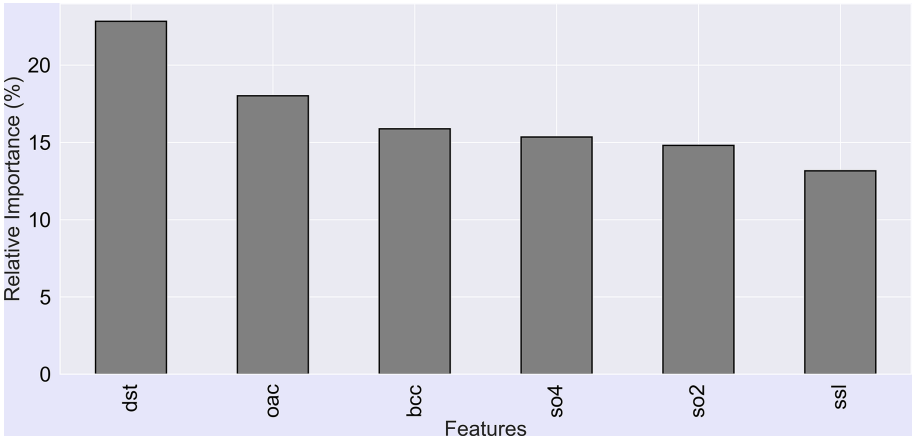

Figure 10. Relative importance of the predictor variables, i.e. the degree of influence of each aerosol-type column mass density on the model decision-making. dst – Dust, oac – Organic Carbon, ssl – Sea-Salt, SO_2 – Sulfate SO_2 – Sulfur dioxide (precursor of SO_4), bcc – Black Carbon.

Table 4. Performance metrics values of the trained model applied to the test and the train (within parenthesis) dataset to predict aerosol optical regimes based on aerosol-type column mass density.

Clusters	Precision	Recall	F_1-score	Support (N)
0	0.62 (0.89)	0.62 (0.78)	0.62 (0.83)	361 (909)
1	0.68 (0.86)	0.70 (0.94)	0.69 (0.90)	517 (1130)
2	0.62 (0.92)	0.60 (0.76)	0.61 (0.83)	47 (106)
3	0.76 (0.93)	0.73 (0.94)	0.74 (0.94)	206 (429)
4	0.68 (0.91)	0.69 (0.93)	0.69 (0.92)	162 (442)

model precision varied within the specific optical regimes (ex., non-dust) and among optical regimes (dust, non-dust). It showed higher precision in identifying C1 than C0, the two dust regimes. Among the non-dust regime clusters, the lowest precision obtained was 0.62 for the prediction of C2; nevertheless, this precision is still a promising outcome considering the limited number of samples of this cluster available for the training process. Given its strong absorption nature, mislabeling the C2 aerosol regime would translate into high error in optical properties prescription; therefore, as mentioned, extra training is required to improve the model prediction for C2 occurrence.

Figure 10 illustrates the relative importance of the predictor variables for the grids consisting of the AERONET sites, highlighting the influence of each aerosol-type column mass density on the model's decision-making. The results indicate that the presence of dust over the Iberian Peninsula is the primary factor affecting the aerosol optical properties in this region. This finding aligns with actual conditions, as the transport of Saharan dust to the peninsula is the main driver of aerosol optical properties variability in the area. Dust is followed by organic carbon, sea salt, and sulfate aerosol types. Organic carbon relevance is associated with biomass burning, a critical aerosol source during the dry season. Interestingly, black carbon column mass density did not rank among the top predictors. Despite the expectation that black carbon might serve as a significant indicator of the aerosol optical regime due to its association with smoke-influenced aerosols. There is considerable uncertainty in black carbon simulations in atmospheric chemistry models, including reanalyses such as MERRA-2, which may hinder its effectiveness in predicting the aerosol regime observed at AERONET monitoring sites.

We also managed to calculate the relative importance of the predictors from Table 1 in the cluster prediction; the result is presented in the supplement (Fig. S2). Consistency can be observed between the score scale from Fig. S2 and that derived from MERRA-2 with respect to aerosol types (Fig. 10). In Fig. 10, dust (dst) mass variability emerges as the most influential factor in determining which cluster should be applied. In the Fig. S2 figure, which presents the importance of the optical parameters from Table 1 for clustering, the scores appear well distributed, with a maximum value close to 0.1. Nevertheless, it is evident that higher wavelengths (near-infrared at 870 and 1020 nm) and specific optical parameters – namely the Asymmetry Parameter and the Linear Depolarization Ratio – exhibit the greatest importance, as they are most effective in distinguishing dust from other aerosol types.

3.3 Application: case studies

From the testing dataset, we selected some case studies that significantly impacted local populations, garnered media attention, and represented different aerosol scenarios in the Iberian Peninsula. This selection provides a visual (qualitative) demonstration of the model's predicting capability (Table 5).

We set our trained model to prescribe the spatial distribution of aerosol optical regimes (clusters) that best fit vari-

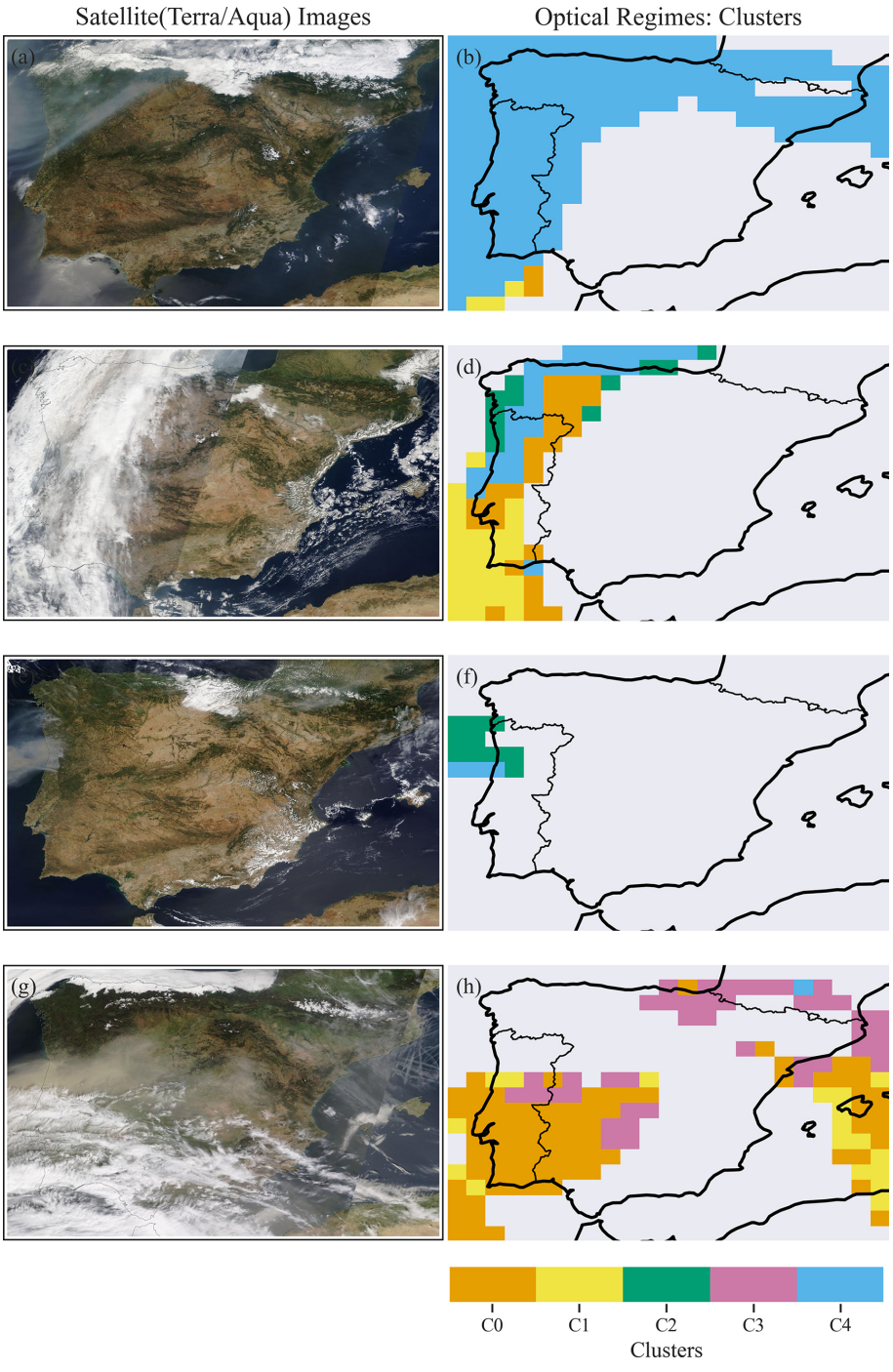

Figure 11. Case studies of distinct aerosol scenarios over the Iberian Peninsula selected to test our machine-learning based approach to predict the best optical property regime: **(a, b)** Case 01 on 27 June 2023; **(c, d)** Case 02 on 16 October 2017; **(e, f)** Case 03 on 11 August 2016; **(g, h)** Case 04 on 17 March 2022. On the left side, MODIS Terra and Aqua/NASA True color satellite images (https://wvs.earthdata.nasa.gov, last access: 1 April 2026); and on the right the cluster spatial distribution prescribed by the model.

ous scenarios based on MERRA-2 aerosol-type column mass density. The results for all cases studied are presented in Fig. 11. To minimize uncertainties associated with the estimates of aerosol absorptivity, AERONET SSA retrievals are limited to cases where the AOD at 440 nm exceeds 0.4 (Dubovik and King, 2000; Holben et al., 2006). Therefore, the discussion of the optical regime prescriptions was focused on areas where AOD was above this threshold. The uncertainty in retrieved SSA is ~ 0.03 at AOD at 440 nm $= 0.4$ and decreases at higher AOD levels (Sinyuk et al., 2020).

Table 5. List of case studies of aerosols high loading events over Iberian Peninsula selected to highlight as examples of the classifier trained model application.

Case study	Date	Nature (reference link)
01	27 June 2023	Smoke[1]
02	16 October 2017	Dust and Smoke[2]
03	11 August 2016	Smoke[3]
04	17 March 2022	Dust[4]

[1] https://earthobservatory.nasa.gov/images/151507/canadian-smoke-reaches-europe (last access: 1 April 2026); [2] https://atmosphere.copernicus.eu/saharan-dust-and-smoke-over-france-and-uk (last access: 1 April 2026); [3] https://earthobservatory.nasa.gov/images/88552/fires-rage-in-portugal (last access: 1 April 2026); [4] https://earthobservatory.nasa.gov/images/149645/dusty-storm-clouds-over-europe (last access: 1 April 2026).

For our regional analysis, we used the MERRA-2 AOD field as a reference, since AERONET provides local AOD at specific sites. Figure S1 in the Supplement exhibits as example the seasonal cycle aerosol AOD at 550 nm over the Iberian Peninsula. Given that the prescription is done based on a map of the combination of aerosol types column density from models, in this case MERRA-2, the only way to filter areas across the Iberian Peninsula where AOD at 440 nm > 0.4 is to use the AOD field from MERRA-2.

Case 01 occurred from 1 to 25 June 2023, coinciding with large-scale wildfire events in Quebec, Canada. A substantial portion of smoke from these wildfires crossed the Atlantic Ocean and reached Western Europe, especially the Iberian Peninsula, resulting in darkened skies in the affected countries. Our trained model predicted that the most suitable aerosol optical regime for the areas impacted by the smoke (Portugal, Western, and Northern Spain) is C4, which corroborates our previous discussion associating the C4 optical regime with regional smoke.

Case 02 features an emblematic event on 16 October 2017, marked by a simultaneous massive wildfire in central and northern Portugal and a strong dust transport from North Africa via the south of Portugal. The path connecting the smoke and dust produced a strong northward transport affecting the United Kingdom, influenced by the synoptic conditions associated with the ex-hurricane Ophelia, located just north of the Iberian Peninsula (Osborne et al., 2019). The optical regime prescription identified the C4 cluster as the appropriate regime from central Portugal northward to the UK. Meanwhile, the area affected by dust, spanning from North Africa to southern and central Portugal, was characterized by a mix of C0 and C1, the clusters associated with dust regimes. As the dust plume arrived in Portugal, the model indicated a gradual transition from C1, indicative of pure dust, to C0, which represents conditions of dust mixed with smoke (Gómez-Amo et al., 2017). The random distribution of C2 within the larger C4 regions likely reflects the model's response to the specific conditions dictated by the aerosol-type column mass densities. This could suggest patches of high-absorbing aerosol-type within a less-absorbing large-scale smoke plume, although there is insufficient evidence to draw definitive conclusions.

Case 03, dated 11 August 2016, involved strong wildfire emissions in northern Portugal. Most of the smoke was transported toward the Atlantic Ocean, while the remainder of the peninsula experienced low aerosol loading conditions. Consistent with fresh smoke aerosol scenarios, the model prescribed the C2 optical regime, the highest absorbing cluster. In strong biomass burning events, especially at the early stage of the emission process, the ratio of elemental carbon to organic carbon is usually high, which has been shown to explain the high absorption features of fresh smoke plume (Schwink et al., 2024). Additionally, previous studies have also shown that Brown Carbon (BrC) absorption is strongest in fresh smoke plumes and decreases with atmospheric processing (Saleh et al., 2014; Pokhrel et al., 2017).

Case 04 pertains to an extreme Saharan dust transport that affected most of the Iberian Peninsula on 15–17 March 2022. During this event, the 24 h average concentration of PM2.5 reached as high as 700 $\mu g\,m^{-3}$ in parts of Spain (Rodríguez and López-Darias, 2024). The pollution episode was dominated by dust, and indeed, the model prescribed the optical regimes C0 and C1, which indicate pure dust and dusty conditions for most of the Iberian Peninsula. This demonstrates our approach's capability to differentiate specific scenarios within dust regimes. For non-dust regimes such as C2, a highly absorbing regime, we would not expect to see widespread prescriptions, as we hypothesize that it is associated with fresh, high-absorbing pollution plumes.

Figure 6, depicting the occurrence of each cluster across the Iberian Peninsula, corroborates our hypothesis by indicating that the C2 regime is mainly present in specific areas where aerosol loading increases are primarily attributed to biomass burning, such as the western lowlands of the Iberian Peninsula (Evora, Badajoz, and Caceres) and in the Galicia region (Coruna). The C3 optical regime was not linked to large-scale dust transport or smoke plumes across the Iberian Peninsula, suggesting it might be associated with high levels of local or regional pollution. Figure 6 shows that the C3 regime is commonly observed throughout the year in the eastern portion of the Iberian Peninsula. The results of these case studies, combined with performance evaluations, highlight the capability and potential of this machine-learning approach, which uses clustering and random forest classification to prescribe optical models from aerosol-type columnar mass density to calculate aerosol particles' direct radiative effect in atmospheric models. By constraining modelling with observational aerosol optical data, we can help mitigate the known uncertainties related to aerosol direct radiative forcing.

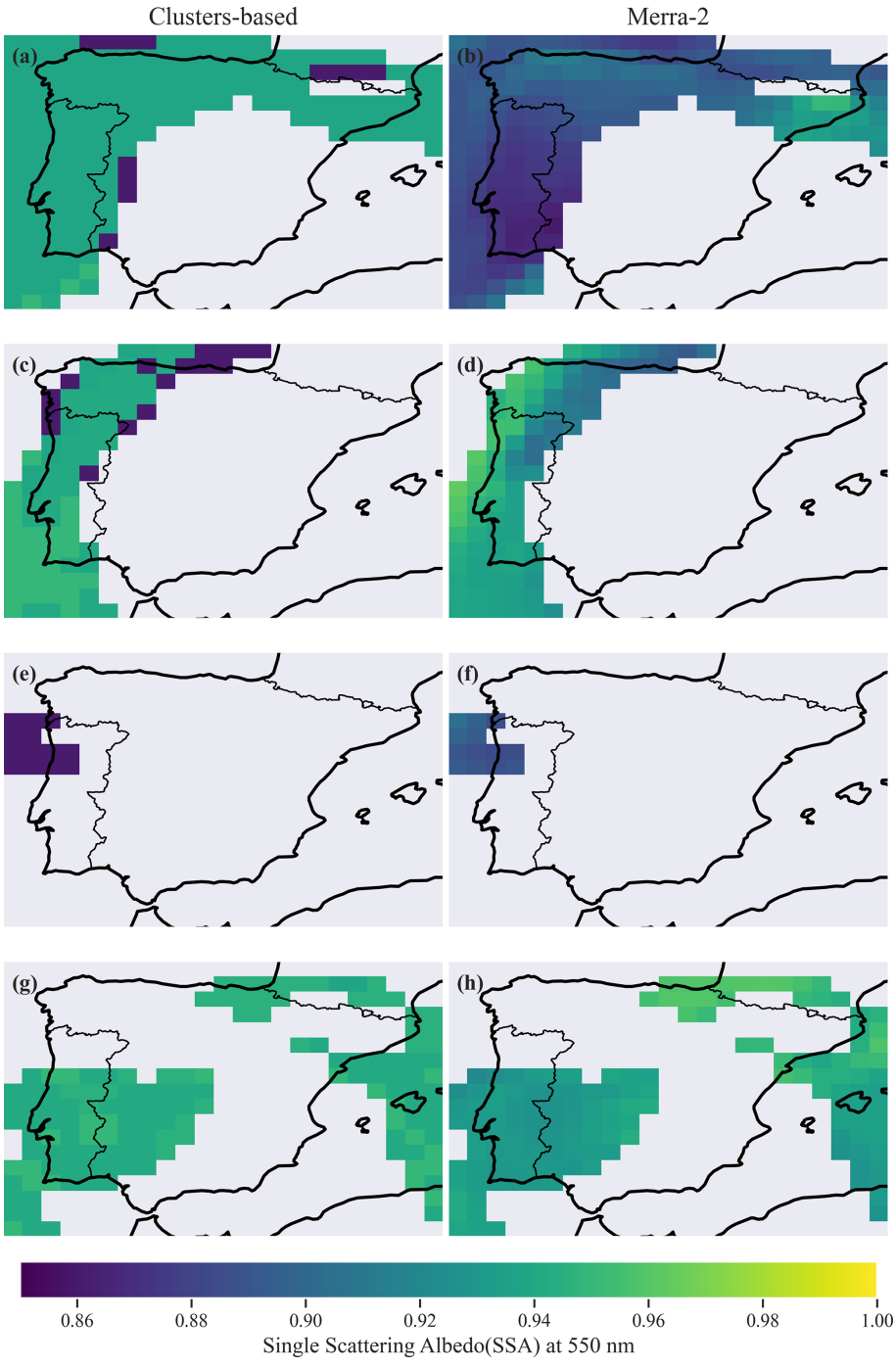

Figure 12. Single Scattering Albedo (SSA) prescription based on the current study approach **(a, c, e, g)** and that simulated by MERRA-2 **(b, d, f, h)** for the selected case studies of Table 5: **(a, b)** Case 01 on 27 June 2023; **(c, d)** Case 02 on 16 October 2017; **(e, f)** Case 03 on 11 August 2016; **(g, h)** Case 04 on 17 March 2022.

Figure 12 shows the single scattering albedo at 550 nm, comparing the current approach and MERRA-2 reanalysis results. The MERRA-2 columnar total SSA was calculated based on the ratio of total scattering aerosol optical depth to total extinction aerosol optical depth, both provided in MERRA-2 aerosol products. For smoke scenarios on 27 June 2023, MERRA-2 indicated a more absorbing optical regime (SSA at 550 nm ∼ 0.86–0.90) compared to the current approach (SSA at 550 nm ∼ 0.95). On this day, the average SSA at 550 nm over the AERONET site in Coruna City, which was directly affected by Canadian smoke, exceeded 0.95. The opposite was observed for the

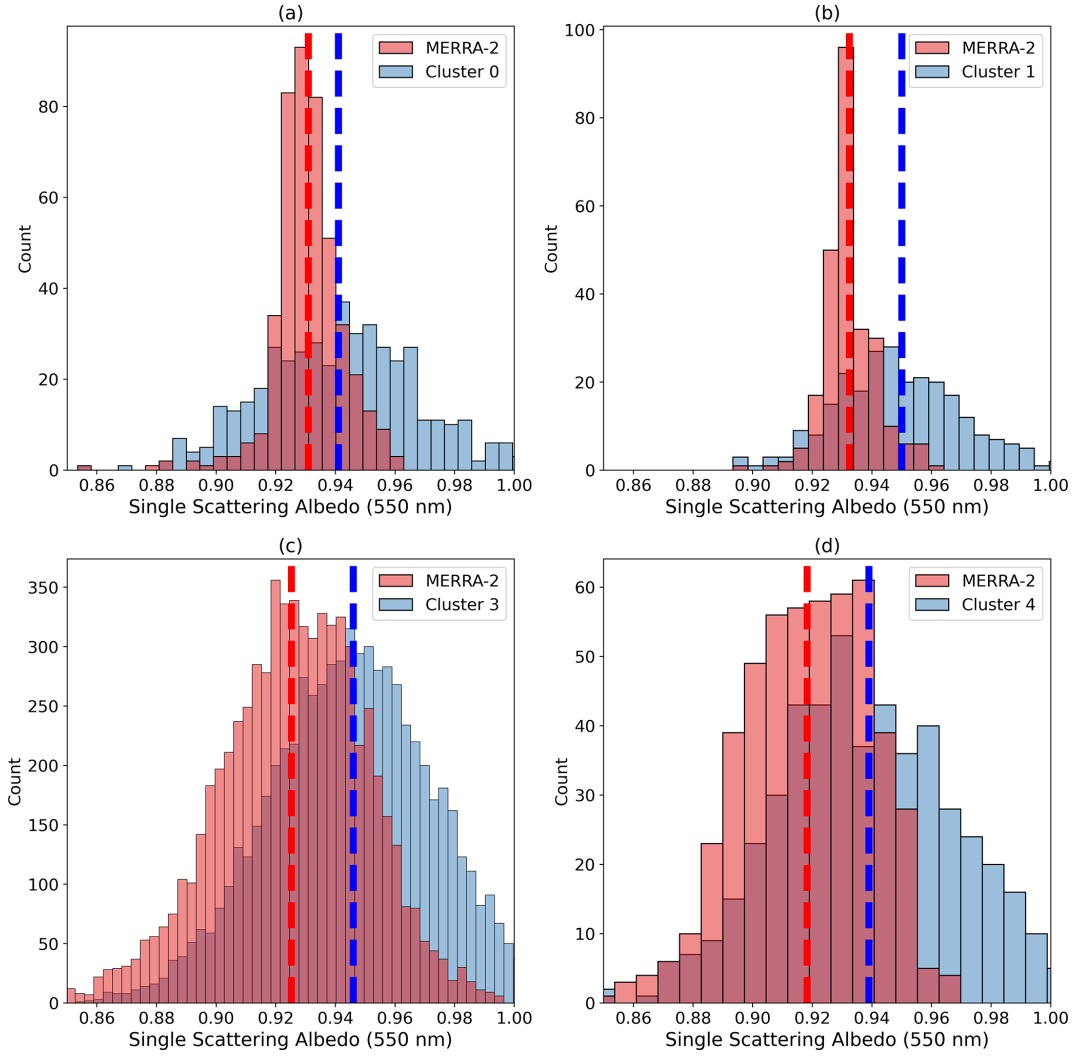

Figure 13. Current study prescription and MERRA-2 simulation of Single Scattering Albedo (SSA) frequency distribution as function of the optical regime (clusters): **(a)** Cluster 0; **(b)** Cluster 1; **(c)** Cluster 3; **(d)** Cluster 4. The dashed lines represent the mean values.

strong smoke emission event that occurred over northern Portugal on 11 August 2016. Current strategy prescribed a much lower SSA, therefore the strongest absorbing regime, when compared with the MERRA-2 calculation. Due to the absence of a site in the northern part of Portugal, we were not able to compare the prescribed and simulated values with AERONET data. For the dust scenario, on 17 March 2022, the current approach prescribed a less absorbing optical regime (SSA at 550 nm $\sim$ 0.94–0.95) compared to MERRA-2, which reported a SSA at 550 nm of roughly 0.92–0.94. The analysis of SSA at 550 nm over AERONET sites affected by the dust event surpassed 0.94. While these cases highlight differences between the prescriptions based on the clusters and MERRA-2 results, they are only sufficient to warrant further investigation. To gain a statistical perspective on whether the findings from these case studies are isolated incidents or indicative of a trend, we compare a much larger sample of MERRA-2 SSA at 550 nm across various AERONET sites in the Iberian Peninsula using the clusters approach. We focused only on MERRA-2 aerosol scenarios for AOD at 550 nm larger than 0.3, which correspond to AOD higher than 0.4 at 440 nm previously mentioned, and conducted the comparison segmented by the optical regimes defined by the clusters.

Figure 13 shows the count distribution of MERRA-2 SSA at 550 nm for the aerosol regimes represented by the clusters C0, C1, C3, and C4, as classified by the random forest classifier we developed. Histograms of clusters of SSA at 550 nm presented in Fig. 13 were generated following a Gaussian distribution, considering the cluster average as the central value of each optical regime cluster and standard deviation as the typical spread. A similar analysis was conducted for the Angstrom Exponent (Fig. 14) to evaluate aspects related to particle size distribution. Based on Fig. 13,

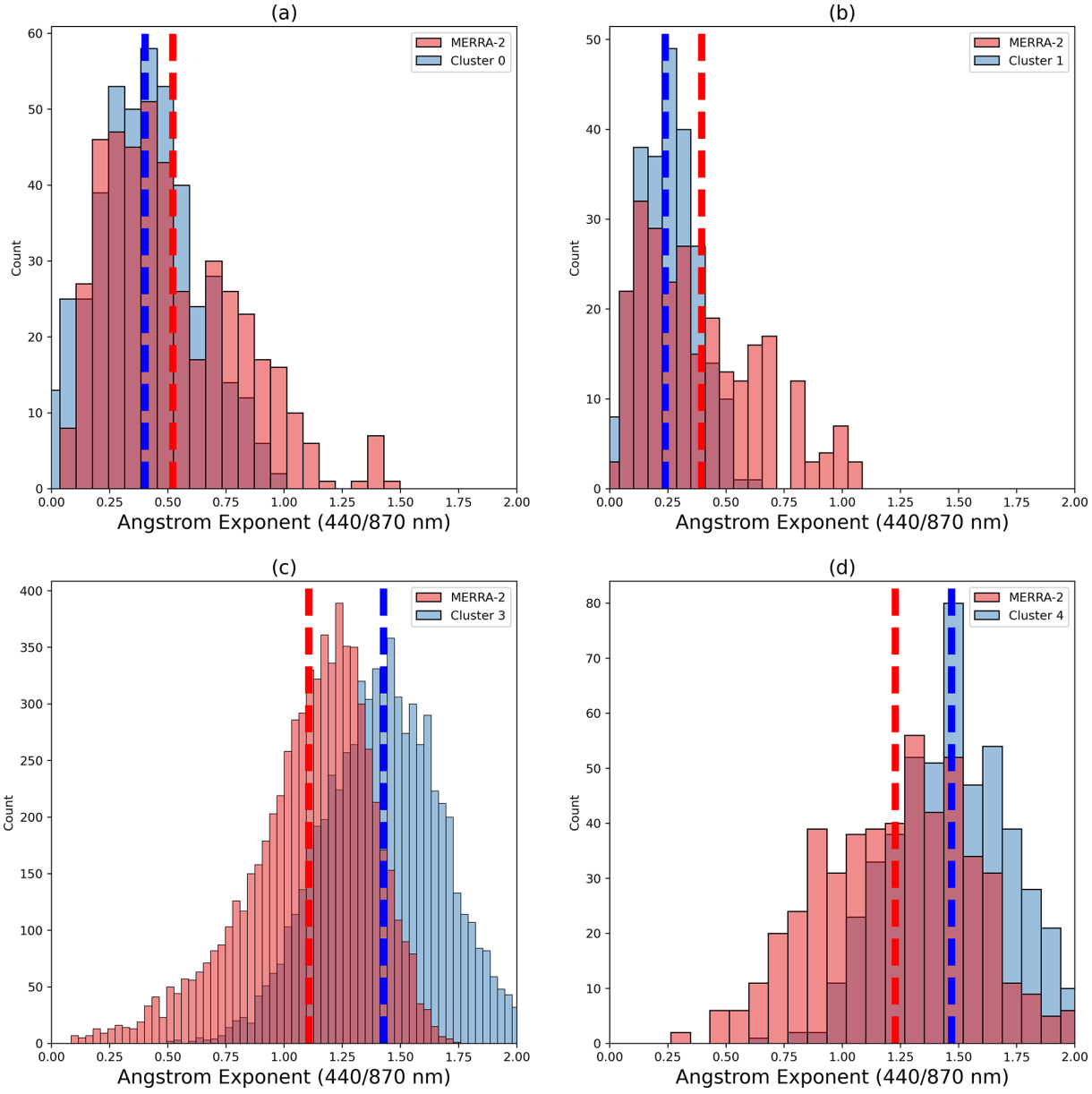

Figure 14. Current study prescription and MERRA-2 simulation of Angstrom Exponent (AE) frequency distribution as function of the optical regime (clusters): **(a)** Cluster 0; **(b)** Cluster 1; **(c)** Cluster 3; **(d)** Cluster 4. The dashed lines represent the mean values.

we found that, on average, our aerosol optical regime prescription based on the clusters (AERONET) is less absorbing than MERRA-2 for aerosol regimes C0, C1, C3, and C4. More significant differences are observed for C1, C3, and C4. Cluster C1 corresponds to a dust scenario closer to pure dust, while C4 is dominated by smoke. Regarding the particle size indicator (AE), it was observed that MERRA-2 has a lower contribution of coarse particles in the dust regimes compared to the cluster-based prescriptions (Fig. 14a and b). This finding aligns with Adebiyi et al. (2023), who noted that climate models tend to underestimate large dust particles, mainly when representing North African dust plumes. Conversely, for the non-dust regimes (C3, C4), MERRA-2 shows a larger relative contribution of coarse particles than the clusters-based prescription (Fig. 14c and d). Figure 15 shows the results for C2. For this specific regime, on average, prescriptions based on the cluster (AERONET) are more absorbing than MERRA-2, opposite to the findings of the other clusters. Regarding AE, under the C2 regime, MERRA-2's mean AE is lower than that prescribed from the cluster, suggesting a lower relative contribution of fine mode in the reanalysis simulations. This is similar to the findings related to the two other fine-mode dominant regimes (C3 and C4).

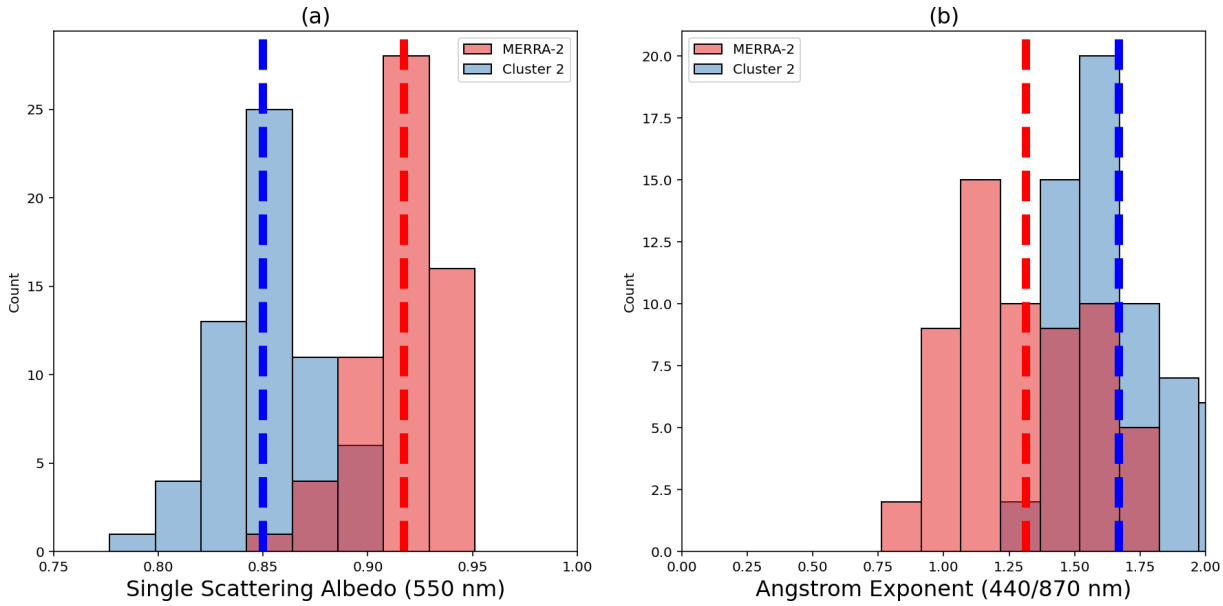

Figure 15. Current study prescription and MERRA-2 simulation of **(a)** Single Scattering Albedo and **(b)** Angstrom Exponent (AE) frequency distribution for the Cluster 2 scenario. The dashed lines represent the mean values.

As demonstrated by the SSA and AE distributions (Fig. 13–15) and evaluated from Tables 1 and 4, the model can also predict the occurrence of the minority cluster C2 (3 %–4 % of samples). The model preserves the distribution of optical properties of less frequent aerosol regimes while capturing MERRA-2 features without the need for explicit class imbalance treatment, with C2's highly absorbing and dominant fine mode conditions reflected in both SSA and AE predictions, with the distributions of values across clusters showing coherence with MERRA-2 values. With C2's highly absorbing and dominant fine mode conditions reflected in both SSA and AE predictions, the distributions across clusters demonstrate agreement between expected and observed distribution values.

4 Conclusions

This study emphasizes the importance of observational-based research to constrain the prescription of aerosol-intensive properties in atmospheric models. We aimed to characterize the typical aerosol intensive optical properties affecting the Iberian Peninsula (IP) using data from the atmospheric column AERONET sky inversion products. We employed K-means clustering to analyze historical aerosol intensive properties across all AERONET sites that operated for at least two years and had the highest quality dataset level (2.0) available. We identified five distinct clusters (C0, C1, C2, C3, and C4) representing different optical regimes, illustrating the predominant aerosol scenarios in the IP. The key difference among these clusters lies in the contribution of coarse-mode particles and their absorption efficiency. Clusters C0 and C1 are dominated by coarse-mode particles and classified as dust regimes due to their association with Saharan dust transport. In particular, the optical properties of C1 closely resemble a pure dust scenario, while C0 indicates a more mixed situation, which we refer to as dusty. On the other hand, clusters C2 and C4 are identified as non-dust regimes, linked to strong and moderate absorption related to smoke plumes. Cluster C3, also a non-dust regime, is more frequently observed in the eastern part of the IP and differs from C4 mainly by having a much lower real part of the refractive index. After identifying the typical aerosol regimes affecting the IP, we utilized aerosol-type columnar mass density data (dust, organic carbon, black carbon, sea salt, and sulfates) from MERRA-2 to predict the aerosol optical regime at each grid point using the supervised learning methodology Random Forest. We tested the performance of the trained model under various aerosol scenarios. The accuracy of the predictions for the aerosol optical regimes ranged from 60 % to 75 %, depending on the regime, with an average accuracy of 70 %. Notably, the accuracy exceeded 90 % when predicting solely dust or non-dust optical regimes.

An analysis of MERRA-2 simulations alongside this study's AERONET cluster-based prescriptions of optical regime indicators, such as absorption (SSA) and size (AE), reveals that MERRA-2 is generally more absorbing for the aerosol optical regimes (C0, C1, C3, and C4) impacting the atmosphere of the Iberian Peninsula, except for the most absorbing regime (C2). Specifically, the reanalysis simulations indicate higher absorption under the non-dust regimes C3 and C4. When examining the relative contributions of fine and coarse modes, the cluster-based prescription indicates

a larger average contribution of coarse particles than the MERRA-2 under dust regimes (C0, C1). Conversely, for the non-dust regimes (C2, C3, C4), MERRA-2 shows a lower relative contribution from the fine mode compared to the clusters-based prescription.

Our findings contribute to enhancing the understanding of the dynamic aerosol optical properties over the Iberian Peninsula and highlight the potential of machine-learning approaches to improve the representation of aerosol radiative forcing in atmospheric models. Many atmospheric modelling systems are not designed to simulate aerosol-intensive microphysical and optical properties in real time. Additionally, computational cost remains a common limitation worldwide. Our approach integrates AERONET-derived intensive properties based on climatological optical regimes to refine the model, coupled with predicted aerosol-type columnar mass density. This integration can help reduce regional uncertainty in the simulation of aerosol radiative forcing.

Nevertheless, we acknowledge that additional research and analysis are necessary to build on the developments and findings presented here. Among the potential limitations and directions for future work, we emphasize the importance of better understanding the impact of AERONET parameter uncertainties on the clustering process, as well as conducting an intercomparison between basic and more advanced clustering approaches. A natural extension of this study would be the development of a comprehensive investigation focused on radiative transfer calculations, within which the proposed method could be thoroughly evaluated.

Code and data availability. All the datasets (AERONET and MERRA-2) used in this study are publicly available and were downloaded from their respective websites (https://aeronet.gsfc.nasa.gov/, last access: 1 April 2026; and https://disc.gsfc.nasa.gov/datasets?project=MERRA-2, last access: 1 April 2026). Code and dataset required to conduct the analyses herein is available at https://doi.org/10.5281/zenodo.14825197 (Rosario, 2025).

Supplement. The supplement related to this article is available online at https://doi.org/10.5194/gmd-19-2691-2026-supplement.

Author contributions. NR, KL and PT designed and performed the research, analyzed the data, and wrote the first version of the paper. MY, SF, LF, OM, HFCV contributed to writing, discussion, review and editing. ICM and AIM conceptualization and coordination of the Project FIRESMOKE, discussion, review and editing.

Competing interests. The contact author has declared that none of the authors has any competing interests.

Disclaimer. Publisher's note: Copernicus Publications remains neutral with regard to jurisdictional claims made in the text, published maps, institutional affiliations, or any other geographical representation in this paper. The authors bear the ultimate responsibility for providing appropriate place names. Views expressed in the text are those of the authors and do not necessarily reflect the views of the publisher.

Acknowledgements. This work was developed as part of the projects FIRESMOKE (https://doi.org/10.54499/PTDC/CTA-MET/3392/2020), LARGEFIRES (https://doi.org/10.54499/2023.17415.ICDT) and of CESAM – Centro de Estudos do Ambiente e do Mar (UID/50017/2025 and LA/P/0094/2020). We thank the AERONET and MERRA-2 PIs and teams for their effort in establishing and maintaining the observational sites and reanalysis products used in this study. We acknowledge the use of imagery from the Worldview Snapshots application (https://wvs.earthdata.nasa.gov, last access: 1 April 2026), part of the Earth Observing System Data and Information System (EOSDIS). Finally, we would like to acknowledge the constructive review comments by the two anonymous reviewers and the editor.

Financial support. The authors acknowledge the financial support of FCT – Science and Technology Portuguese Foundation I.P., which funded the projects FIRESMOKE (https://doi.org/10.54499/PTDC/CTA-MET/3392/2020) and LARGEFIRES (https://doi.org/10.54499/2023.17415.ICDT), through national funds. This work was also funded by national funds through FCT, under the project CESAM-Centro de Estudos do Ambiente e do Mar, references UID/50017/2025 (https://doi.org/10.54499/UID/50017/2025) and LA/P/0094/2020 (https://doi.org/10.54499/LA/P/0094/2020). The authors also acknowledge the financial support from the Conselho Nacional de Desenvolvimento Científico e Tecnológico (CNPq, Brazil) under grant agreement nos. 441851/2023-1, 172486/2023-8, and 315349/2023-9.

Review statement. This paper was edited by Klaus Klingmüller and reviewed by two anonymous referees.

References

Abraham, A., Pedregosa, F., Eickenberg, M., Gervais, P., Mueller, A., Kossaifi, J., Gramfort, A., Thirion, B., and Varoquaux, G.: Machine Learning for Neuroimaging with Scikit-Learn, Front. Neuroinform., 8, 14, https://doi.org/10.3389/fninf.2014.00014, 2014.

Adebiyi, A. A., Huang, Y., and Samset, B. H.: Observations suggest that North African dust absorbs less solar radiation than models estimate, Commun. Earth Environ., 4, 168, https://doi.org/10.1038/s43247-023-00825-2, 2023.

Alvarez, A., Lecina-Diaz, J., Batllori, E., Duane, A., Brotons, L., and Retana, J.: Spatiotemporal patterns and

drivers of extreme fire severity in Spain for the period 1985–2018, Agr. Forest Meteorol., 358, 110185, https://doi.org/10.1016/j.agrformet.2024.110185, 2024.

Asfaw, H. W., McGee, T. K., and Correia, F. J.: Wildfire preparedness and response during the 2016 Arouca wildfires in rural Portugal, Int. J. Disast. Risk Reduct., 73, 102895, https://doi.org/10.1016/j.ijdrr.2022.102895, 2022.

Breiman, L.: Random Forests, Mach. Learn., 45, 5–32, https://doi.org/10.1023/a:1010933404324, 2001.

Brown, H., Liu, X., Pokhrel, R., Murphy, S., Lu, Z., Saleh, R., Mielonen, T., Kokkola, H., Bergman, T., Myhre, G., Skeie, R. B., Watson-Paris, D., Stier, P., Johnson, B., Bellouin, N., Schulz, M., Vakkari, V., Beukes, J. P., van Zyl, P. G., Liu, S., and Chand, D.: Biomass burning aerosols in most climate models are too absorbing, Nat. Commun., 12, 277, https://doi.org/10.1038/s41467-020-20482-9, 2021.

Buchard, V. J., Randles, C. A., da Silva, A. M., Darmenov, A., Colarco, P. R., Govindaraju, R., Ferrare, R. A., Hair, J., Beyersdorf, A., Ziemba, L. D., and Yu, H.: The MERRA-2 Aerosol Reanalysis, 1980 Onward. Part II: Evaluation and Case Studies, J. Climate, 30, 6851–6872, https://doi.org/10.1175/JCLI-D-16-0613.1, 2017.

Cachorro, V. E., Burgos, M. A., Mateos, D., Toledano, C., Bennouna, Y., Torres, B., de Frutos, Á. M., and Herguedas, Á.: Inventory of African desert dust events in the north-central Iberian Peninsula in 2003–2014 based on sun-photometer–AERONET and particulate-mass–EMEP data, Atmos. Chem. Phys., 16, 8227–8248, https://doi.org/10.5194/acp-16-8227-2016, 2016.

Chen, G., Wang, J., Wang, Y., Wang, J., Jin, Y., and Cheng, Y.: An aerosol optical module with observation-constrained black carbon properties for global climate models, J. Adv. Model. Earth Syst., 15, e2022MS003501, https://doi.org/10.1029/2022MS003501, 2023.

Chin, M., Ginoux, P., Kinne, S., Torres, O., Holben, B. N., Duncan, B. N., Martin, R. V., Logan, J. A., Higurashi, A., and Nakajima, T.: Tropospheric aerosol optical thickness from the GOCART model and comparisons with satellite and sun photometer measurements, J. Atmos. Sci., 59, 461–483, https://doi.org/10.1175/1520-0469(2002)059<0461:taotft>2.0.co;2, 2002.

Colarco, P., Da Silva, A., Chin, M., and Diehl, T.: Online simulations of global aerosol distributions in the NASA GEOS-4 model and comparisons to satellite and ground-based aerosol optical depth, J. Geophys. Res.-Atmos., 115, D14207, https://doi.org/10.1029/2009JD012820, 2010.

Colarco, P. R., Nowottnick, E. P., Randles, C. A., Yi, B., Yang, P., Kim, K. M., Smith, J. A., and Bardeen, C. G.: Impact of radiatively interactive dust aerosols in the NASA GEOS-5 climate model: Sensitivity to dust particle shape and refractive index, J. Geophys. Res.-Atmos., 119, 753–786, https://doi.org/10.1002/2013JD020046, 2014.

Dubovik, O. and King, M. D.: A flexible inversion algorithm for retrieval of aerosol optical properties from Sun and sky radiance measurements, J. Geophys. Res., 105, 20673–20696, https://doi.org/10.1029/2000JD900282, 2000.

Dubovik, O., Holben, B., Eck, T. F., Smirnov, A., Kaufman, Y. J., King, M. D., Tanré, D., and Slutsker, I.: Variability of Absorption and Optical Properties of Key Aerosol Types Observed in Worldwide Locations, J. Atmos. Sci., 59, 590–608, https://doi.org/10.1175/1520-0469(2002)059<0590:VOAAOP>2.0.CO;2, 2002.

Eck, T. F., Holben, B. N., Reid, J. S., Dubovik, O., Smirnov, A., O'Neill, N. T., Slutsker, I., and Kinne, S.: Wavelength dependence of the optical depth of biomass burning, urban, and desert dust aerosols, J. Geophys. Res., 104, 31333–31349, https://doi.org/10.1029/1999jd900923, 1999.

Elias, T. G., Silva, A. M., Figueira, M. J., Belo, N., Pereira, S., Formenti, P., and Helas, G.: Aerosol extinction and absorption in Évora, Portugal, during the European 2003 summer heat wave, in: Proc. SPIE 5571, Remote Sensing of Clouds and the Atmosphere IX, https://doi.org/10.1117/12.566579, 2004.

Ermitão, T., Páscoa, P., Trigo, I., Alonso, C., and Gouveia, C.: Mapping the Most Susceptible Regions to Fire in Portugal, Fire, 6, 254, https://doi.org/10.3390/fire6070254, 2023.

Fan, Y., Sun, X., Huang, H., Ti, R., and Liu, X.: The primary aerosol models and distribution characteristics over China based on the AERONET data, J. Quant. Spectrosc. Ra., 275, 107888, https://doi.org/10.1016/j.jqsrt.2021.107888, 2021.

Gelaro, R., McCarty, W., Suárez, M. J., Todling, R., Molod, A., Takacs, L., Randles, C. A., Darmenov, A., Bosilovich, M. G., Reichle, R., Wargan, K., Coy, L., Cullather, R., Draper, C., Akella, S., Buchard, V., Conaty, A., da Silva, A. M., Gu, W., Postylyakov, S., Keller, J. H., Gelaro, R., and Pawson, S.: The Modern-Era Retrospective Analysis for Research and Applications, Version 2 (MERRA-2), J. Climate, 30, 5419–5454, https://doi.org/10.1175/JCLI-D-16-0758.1, 2017.

Giles, D. M., Sinyuk, A., Sorokin, M. G., Schafer, J. S., Smirnov, A., Slutsker, I., Eck, T. F., Holben, B. N., Lewis, J. R., Campbell, J. R., Welton, E. J., Korkin, S. V., and Lyapustin, A. I.: Advancements in the Aerosol Robotic Network (AERONET) Version 3 database – automated near-real-time quality control algorithm with improved cloud screening for Sun photometer aerosol optical depth (AOD) measurements, Atmos. Meas. Tech., 12, 169–209, https://doi.org/10.5194/amt-12-169-2019, 2019.

Gliß, J., Mortier, A., Schulz, M., Andrews, E., Balkanski, Y., Bauer, S. E., Benedictow, A. M. K., Bian, H., Checa-Garcia, R., Chin, M., Ginoux, P., Griesfeller, J. J., Heckel, A., Kipling, Z., Kirkevåg, A., Kokkola, H., Laj, P., Le Sager, P., Lund, M. T., Lund Myhre, C., Matsui, H., Myhre, G., Neubauer, D., van Noije, T., North, P., Olivié, D. J. L., Rémy, S., Sogacheva, L., Takemura, T., Tsigaridis, K., and Tsyro, S. G.: AeroCom phase III multi-model evaluation of the aerosol life cycle and optical properties using ground- and space-based remote sensing as well as surface in situ observations, Atmos. Chem. Phys., 21, 87–128, https://doi.org/10.5194/acp-21-87-2021, 2021.

Gómez-Amo, J. L., Estellés, V., Marcos, C., Segura, S., Esteve, A. R., Pedrós, R., Utrillas, M. P., and Martínez-Lozano, J. A.: Impact of dust and smoke mixing on column-integrated aerosol properties from observations during a severe wildfire episode over Valencia (Spain), Sci. Total Environ., 599–600, 2121–2134, https://doi.org/10.1016/j.scitotenv.2017.05.041, 2017.

Groß, S., Tesche, M., Freudenthaler, V., Toledano, C., Wiegner, M., Ansmann, A., Althausen, D., and Seefeldner, M.: Characterization of Saharan dust, marine aerosols and mixtures of biomass-burning aerosols and dust by means of multi-wavelength depolarization and Raman lidar measurements during SAMUM 2, Tellus B, 63, 706–724, https://doi.org/10.1111/j.1600-0889.2011.00556.x, 2011.

Gupta, P., Remer, L. A., Levy, R. C., and Mattoo, S.: Validation of MODIS 3 km land aerosol optical depth from NASA's EOS Terra and Aqua missions, Atmos. Meas. Tech., 11, 3145–3159, https://doi.org/10.5194/amt-11-3145-2018, 2018.

Hammed, R. A., Alawode, G. L., Montoya, L. E., Krasovskiy, A., and Kraxner, F.: Exploring Drivers of Wildfires in Spain, Land, 13, 762, https://doi.org/10.3390/land13060762, 2024.

Hess, M., Koepke, P., and Schult, I.: Optical properties of aerosols and clouds: The software package OPAC, B. Am. Meteorol. Soc., 79, 831–844, 1998.

Hoelzemann, J. J., Longo, K. M., Fonseca, R. M., do Rosario, N. M. E., Elbern, H., Freitas, S. R., and Pires, C.: Regional representativity of AERONET observation sites during the biomass burning season in South America determined by correlation studies with MODIS Aerosol Optical Depth, J. Geophys. Res., 114, D13301, https://doi.org/10.1029/2008jd010369, 2009.

Holben, B. N., Eck, T. F., Slutsker, I., Tanre, D., Buis, J. P., Setzer, A., Vermote, E., Reagan, J. A., Kaufman, Y. J., Nakajima, T., Lavenu, F., Jankowiak, I., and Smirnov, A.: AERONET– A Federated Instrument Network and Data Archive for Aerosol Characterization, Remote Sens. Environ., 66, 1–16, https://doi.org/10.1016/s0034-4257(98)00031-5, 1998.

Holben, B. N., Eck, T. F., Slutsker, I., Smirnov, A., Sinyuk, A., Schafer, J., Giles, D., and Dubovik, O.: AERONET's version 2.0 quality assurance criteria, Proc. SPIE, 6408, 64080Q, https://doi.org/10.1117/12.706524, 2006.

Illingworth, A. J., Barker, H. W., Beljaars, A., Ceccaldi, M., Chepfer, H., Clerbaux, N., Cole, J., Delanoë, J., Domenech, C., Donovan, D. P., Fukuda, S., Hirakata, M., Hogan, R. J., Huenerbein, A., Kollias, P., Kubota, T., Nakajima, T., Nakajima, T. Y., Nishizawa, T., Ohno, Y., Okada, K., Oki, R., Sato, K., Satoh, M., Shephard, M. W., Velázquez-Blázquez, A., Wandinger, U., Wehr, T., and van Zadelhoff, G. J.: The EarthCARE Satellite: The Next Step Forward in Global Measurements of Clouds, Aerosols, Precipitation, and Radiation, B. Am. Meteorol. Soc., 96, 1311–1332, https://doi.org/10.1175/BAMS-D-12-00227.1, 2015.

IPCC: Climate Change 2021 – the Physical Science Basis, in: Contribution of Working Group I to the Sixth Assessment Report of the Intergovernmental Panel on Climate Change, edited by: Masson-Delmotte, V., Zhai, P., Pirani, A., Connors, S. L., Péan, C., Berger, S., Caud, N., Chen, Y., Goldfarb, L., Gomis, M. I., Huang, M., Leitzell, K., Lonnoy, E., Matthews, J. B. R., Maycock, T. K., Waterfield, T., Yelekçi, O., Yu, R., and Zhou, B., Cambridge University Press, Cambridge, UK and New York, NY, USA, https://doi.org/10.1017/9781009157896, 2021.

Kanitz, T., Ansmann, A., Engelmann, R., and Althausen, D.: North-south cross sections of the vertical aerosol distribution over the Atlantic Ocean from multiwavelength Raman/polarization lidar during Polarstern cruises, J. Geophys. Res.-Atmos., 118, 2643–2655, https://doi.org/10.1002/jgrd.50273, 2013.

Kim, D. and Ramanathan, V.: Solar Radiation Budget and Radiative Forcing Due to Aerosols and Clouds, J. Geophys. Res.-Atmos., 113, D02203, https://doi.org/10.1029/2007JD008434, 2008.

Koepke, P., Hess, M., Schult, I., and Shettle, E. P.: Global aerosol data set, Rep. 243, Max-Planck-Inst. für Meteorol., Hamburg, Germany, https://mpimet.mpg.de/fileadmin/publikationen/Reports/max_scirep_243.pdf (last access: 1 April 2026), 1997.

Krishnaveni, S. A., Madhavan, B. L., and Ratnam, M. V.: Aerosol classification using fuzzy clustering over a tropical rural site, Atmos. Res., 282, 106518, https://doi.org/10.1016/j.atmosres.2022.106518, 2023.

Levy, R. C., Remer, L. A., and Dubovik, O.: Global aerosol optical properties and application to Moderate Resolution Imaging Spectroradiometer aerosol retrieval over land, J. Geophys. Res.-Atmos., 112, D13210, https://doi.org/10.1029/2006JD007815, 2007.

Levy, R. C., Remer, L. A., Kleidman, R. G., Mattoo, S., Ichoku, C., Kahn, R., and Eck, T. F.: Global evaluation of the Collection 5 MODIS dark-target aerosol products over land, Atmos. Chem. Phys., 10, 10399–10420, https://doi.org/10.5194/acp-10-10399-2010, 2010.

Li, J., Liu, L., Lacis, A. A., and Carlson, B. E.: An optimal fitting approach to improve the GISS ModelE aerosol optical property parameterization using AERONET data, J. Geophys. Res., 115, D16211, https://doi.org/10.1029/2010JD013909, 2010.

Li, J., Carlson, B. E., and Yung, Y. L.: Scattering and absorbing aerosols in the climate system, Natl. Rev. Earth Environ., 3, 363–379, https://doi.org/10.1038/s43017-022-00296-7, 2022.

Li, Z., Zhang, Y., Xu, H., Li, K., Dubovik, O., and Goloub, P.: The Fundamental Aerosol Models Over China Region: A Cluster Analysis of the Ground-Based Remote Sensing Measurements of Total Columnar Atmosphere, Geophys. Res. Lett., 46, 4924–4932, 2019.

Martins, J. V., Artaxo, P., Kaufman, Y. J., Castanho, A. D., and Remer, L. A.: Spectral absorption properties of aerosol particles from 350–2500 nm, Geophys. Res. Lett., 36, L13810, https://doi.org/10.1029/2009GL037435, 2009.

Moise, T., Flores, J. M., and Rudich, Y.: Optical properties of secondary organic aerosols and their changes by chemical processes, Chem. Rev., 115, 4400–4439, 2015.

Omar, A. H., Won, J.-G., Winker, D. M., Yoon, S.-C., Dubovik, O., and McCormick, M. P.: Development of global aerosol models using cluster analysis of Aerosol Robotic Network (AERONET) measurements, J. Geophys. Res., 110, D10S14, https://doi.org/10.1029/2004JD004874, 2005.

Osborne, M., Malavelle, F. F., Adam, M., Buxmann, J., Sugier, J., Marenco, F., and Haywood, J.: Saharan dust and biomass burning aerosols during ex-hurricane Ophelia: observations from the new UK lidar and sun-photometer network, Atmos. Chem. Phys., 19, 3557–3578, https://doi.org/10.5194/acp-19-3557-2019, 2019.

Pokhrel, R. P., Beamesderfer, E. R., Wagner, N. L., Langridge, J. M., Lack, D. A., Jayarathne, T., Stone, E. A., Stockwell, C. E., Yokelson, R. J., and Murphy, S. M.: Relative importance of black carbon, brown carbon, and absorption enhancement from clear coatings in biomass burning emissions, Atmos. Chem. Phys., 17, 5063–5078, https://doi.org/10.5194/acp-17-5063-2017, 2017.

Proske, U., Ferrachat, S., and Lohmann, U.: Developing a climatological simplification of aerosols to enter the cloud microphysics of a global climate model, Atmos. Chem. Phys., 24, 5907–5933, https://doi.org/10.5194/acp-24-5907-2024, 2024.

Reid, J. S. and Hobbs, P. V.: Physical and optical properties of young smoke from individual biomass fires in Brazil, J. Geophys. Res., 103, 32013–32030, 1998.

Reid, J. S., Eck, T. F., Christopher, S. A., Koppmann, R., Dubovik, O., Eleuterio, D. P., Holben, B. N., Reid, E. A., and Zhang, J.: A review of biomass burning emissions part III: intensive optical properties of biomass burning particles, Atmos. Chem. Phys., 5, 827–849, https://doi.org/10.5194/acp-5-827-2005, 2005.

Rodríguez, S. and López-Darias, J.: Extreme Saharan dust events expand northward over the Atlantic and Europe, prompting record-breaking PM_{10} and $PM_{2.5}$ episodes, Atmos. Chem. Phys., 24, 12031–12053, https://doi.org/10.5194/acp-24-12031-2024, 2024.

Rosario, N. E.: Machine learning-driven characterization and prescription of aerosol optical properties for atmospheric models, Zenodo [code an data set], https://doi.org/10.5281/zenodo.14825197, 2025.

Rosário, N. E., Longo, K. M., Freitas, S. R., Yamasoe, M. A., and Fonseca, R. M.: Modeling the South American regional smoke plume: aerosol optical depth variability and surface shortwave flux perturbation, Atmos. Chem. Phys., 13, 2923–2938, https://doi.org/10.5194/acp-13-2923-2013, 2013.

Russell, P. B., Kacenelenbogen, M., Livingston, J. M., Hasekamp, O. P., Burton, S. P., Schuster, G. L., Johnson, M. S., Knobelspiesse, K. D., Redemann, J., Ramachandran, S., and Holben, B.: A multiparameter aerosol classification method and its application to retrievals from spaceborne polarimetry, J. Geophys. Res.-Atmos., 119, 9838–9863, https://doi.org/10.1002/2013JD021411, 2014.

Saleh, R., Robinson, E. S., Tkacik, D. S., Ahern, A. T., Liu, S., Aiken, A. C., Sullivan, R. C., Presto, A. A., Dubey, M. K., Yokelson, R. J., Donahue, N. M., and Robinson, A. L.: Brownness of organics in aerosols from biomass burning linked to their black carbon content, Nat. Geosci., 7, 647–650, https://doi.org/10.1038/ngeo2220, 2014.

Samset, B. H., Stjern, C. W., Andrews, E., Kahn, R. A., Myhre, G., Schulz, M., and Schuster, G. L.: Aerosol Absorption: Progress Towards Global and Regional Constraints, Curr. Clim. Change Rep., 4, 65–83, https://doi.org/10.1007/s40641-018-0091-4, 2018.

Sand, M., Samset, B. H., Myhre, G., Gliß, J., Bauer, S. E., Bian, H., Chin, M., Checa-Garcia, R., Ginoux, P., Kipling, Z., Kirkevåg, A., Kokkola, H., Le Sager, P., Lund, M. T., Matsui, H., van Noije, T., Olivié, D. J. L., Remy, S., Schulz, M., Stier, P., Stjern, C. W., Takemura, T., Tsigaridis, K., Tsyro, S. G., and Watson-Parris, D.: Aerosol absorption in global models from AeroCom phase III, Atmos. Chem. Phys., 21, 15929–15947, https://doi.org/10.5194/acp-21-15929-2021, 2021.

Schwink, S. K., Mael, L. E., Dunnington, T. H., Schmid, M. J., Silberstein, J. M., Heck, A., Gotlib, N., Hannigan, M. P., and Vance, M. E.: Impacts of Aging and Relative Humidity on Properties of Biomass Burning Smoke Particles, ACS EST Air, 2, 109–118, https://doi.org/10.1021/acsestair.4c00224, 2024.

Shettle, E. P. and Fenn, R. W.: Models for the aerosols of the lower atmosphere and the effects of humidity variations on their optical properties, Environmental Research Papers No. 676, AFGL-TR-79-0214, Optical Physics Division, Air Force Geophysics Laboratory, Hanscom AFB, MA, USA, 94 pp., https://books.google.com/books?id=JSlkjReviS4C (last access: 1 April 2026), 1979.

Shi, C., Wei, B., and Wei, S.: A quantitative discriminant method of elbow point for the optimal number of clusters in clustering algorithm, J. Wireless Commun. Network, 2021, 31, https://doi.org/10.1186/s13638-021-01910-w, 2021.

Shin, S. K., Tesche, M., Kim, K., Kezoudi, M., Tatarov, B., Müller, D., and Noh, Y.: On the spectral depolarisation and lidar ratio of mineral dust provided in the AERONET version 3 inversion product, Atmos. Chem. Phys., 18, 12735–12746, https://doi.org/10.5194/acp-18-12735-2018, 2018.

Silva, P., Carmo, M., Rio, J., and Novo, I.: Changes in the Seasonality of Fire Activity and Fire Weather in Portugal: Is the Wildfire Season Really Longer?, Meteorology, 2, 74–86, https://doi.org/10.3390/meteorology2010006, 2023.

Sinyuk, A., Holben, B. N., Eck, T. F., Giles, D. M., Slutsker, I., Korkin, S., Schafer, J. S., Smirnov, A., Sorokin, M., and Lyapustin, A.: The AERONET Version 3 aerosol retrieval algorithm, associated uncertainties and comparisons to Version 2, Atmos. Meas. Tech., 13, 3375–3411, https://doi.org/10.5194/amt-13-3375-2020, 2020.

Smirnov, A., Holben, B. N., Kaufman, Y. J., Dubovik, O., Eck, T. F., Slutsker, I., Pietras, C., and Halthore, R. N.: Optical Properties of Atmospheric Aerosol in Maritime Environments, J. Atmos. Sci., 59, 501–523, https://doi.org/10.1175/1520-0469(2002)059<0501:OPOAAI>2.0.CO;2, 2002.

Spencer, R. S., Levy, R. C., Remer, L. A., Mattoo, S., Arnold, G. T., Hlavka, D. L., Meyer, K. G., Marshak, A., Wilcox, E. M., and Platnick, S. E.: Exploring Aerosols near Clouds with High-Spatial-Resolution Aircraft Remote Sensing during SEAC(4)RS, J. Geophys. Res.-Atmos., 124, 2148–2173, 2019.

Toledano, C., Cachorro, V. E., de Frutos, A. M., Sorribas, M., and Prats, N.: Inventory of African Desert Dust Events Over the Southwestern Iberian Peninsula in 2000–2005 with an AERONET Cimel Sun Photometer, J. Geophys. Res., 112, D21201, https://doi.org/10.1029/2006JD008307, 2007.

Zhao, A., Ryder, C. L., and Wilcox, L. J.: How well do the CMIP6 models simulate dust aerosols?, Atmos. Chem. Phys., 22, 2095–2119, https://doi.org/10.5194/acp-22-2095-2022, 2022.

Zhao, G., Tan, T., Zhao, W., Guo, S., Tian, P., and Zhao, C.: A new parameterization scheme for the real part of the ambient urban aerosol refractive index, Atmos. Chem. Phys., 19, 12875–12885, https://doi.org/10.5194/acp-19-12875-2019, 2019.

Zhong, Q., Schutgens, N., van der Werf, G. R., van Noije, T., Bauer, S. E., Tsigaridis, K., Mielonen, T., Checa-Garcia, R., Neubauer, D., Kipling, Z., Kirkevåg, A., Olivié, D. J. L., Kokkola, H., Matsui, H., Ginoux, P., Takemura, T., Le Sager, P., Rémy, S., Bian, H., and Chin, M.: Using modelled relationships and satellite observations to attribute modelled aerosol biases over biomass burning regions, Nat. Commun., 13, 5914, https://doi.org/10.1038/s41467-022-33680-4, 2022.

Zhou, P., Wang, Y., Liu, J., Xu, L., Chen, X., and Zhang, L.: Difference between global and regional aerosol model classifications and associated implications for spaceborne aerosol optical depth retrieval, Atmos. Environ., 300, 119674, https://doi.org/10.1016/j.atmosenv.2023.119674, 2023.